

---

## Chapter 2

# Mirror Design For Optical Telescopes

The reflector mirror is the most important component of an astronomical optical telescope. This chapter provides discussions on the requirements for astronomical optical mirrors; the ways to reduce mirror weight, mirror cost, and mirror materials; the methods of mirror figuring, polishing, and surface coating; the design of mirror support mechanism; the concept of mirror seeing; and the stray light control. Emphasis is placed on various mirror designs for modern large optical telescopes. These include the thin mirror, honeycomb mirror, segmented mirror, and multi-mirror telescope concepts. When discussing all these concepts, important formulas and their restrictions are provided for the reader's reference so that they may use them in their mirror design practice. The discussion on the mirror support system is thorough and comprehensive, including both the positional and flotation support systems. A new mirror support system using a hexapod platform is also introduced. In the stray light control section, a new scattering theory based on the bidirectional reflectance distribution function is also introduced.

## 2.1 Specifications for Optical Mirror Design

### 2.1.1 Fundamental Requirements for Optical Mirrors

An optical astronomical telescope, as a very sensitive light collector, comprises a number of important components. Among these, the reflecting primary mirror is the most important. The telescope efficiency is directly related to its area, its reflectivity, and its surface accuracy. The mirror area and reflectivity have been discussed in Section 1.2.2. The mirror surface accuracy is related to wavefront errors which affect the image Strehl ratio. The image Strehl ratio and the wavefront error were briefly introduced in Section 1.4.3.

To obtain sharp star images, a rigorous tolerance is used for the mirror surface precision. The ideal primary mirror shape is determined through optical design, ray tracing, and system optimization. In geometrical optics, this ideal

surface shape ensures a small acute star image spot in the focal plane. This corresponds to a perfect planar Gaussian wavefront on the aperture plane. However, mirror surface shape imperfection always exists due to the mirror manufacture, mirror support, thermal variation, and other reasons. The wavefront error is twice the mirror surface error due to the double reflection.

Generally, the characteristic mirror surface or wavefront error is expressed by the root mean square (rms) of the distance errors to an ideal mirror or wavefront surface. Statistically, the average value of the errors can be made equal to zero by choosing a best fit reference surface, and the rms then is the standard deviation of the error. The square of the rms error is the variance. The ratio between the rms and the peak error depends on the error distributions. For a uniform error distribution, the peak error is twice the rms value. For a triangular error distribution, the peak error is 3.46 times the rms. For a sine error distribution, the peak error is 2.83 times the rms. The peak of a finite sample from a Gaussian distribution is not fixed; being typically 6 to 8 times the rms. When more than one independent factor (in mathematics, independent error terms are orthogonal to each other) exists, the combined rms error is the root sum square (rss) of the rms errors of individual factors.

According to electromagnetic wave theory, if the wavefront deviates from an ideal one, the radiation energy of the image will be redistributed resulting in: (a) a decrease in image sharpness; (b) an increase in image size; and (c) a decrease in image central energy, and the Strehl ratio of the image decreases.

For an axial symmetrical aperture, the diffraction radiation energy distribution at a position  $P$  is:

$$I(P) = \left( \frac{Aa^2}{\lambda R^2} \right)^2 \left| \int_0^1 \int_0^{2\pi} e^{i(2\pi\phi/\lambda - v\rho \cos(\theta-\psi) - 1/2u\rho^2)} \rho d\rho d\theta \right|^2 \quad (2.1)$$

where  $A$  is the radiation amplitude on the aperture plane,  $\phi$  the wavefront phase error,  $a$  the aperture radius,  $\rho$  and  $\theta$  polar angles in the aperture plane,  $r$  and  $\psi$  polar angles in the image plane,  $z$  the axial distance between the aperture and the image,  $R$  the distance between image position  $P$  and the point to be integrated on the aperture plane,  $u = (2\pi/\lambda)(a/R)^2 z$ , and  $v = (2\pi/\lambda)(a/R)r$ .

Without wavefront aberrations, the maximum on-axis intensity is:

$$I_{\phi=0}(P_{r=0}) = \pi^2 \left( \frac{Aa^2}{\lambda R^2} \right)^2 = \left( \frac{\pi^2 A^4}{\lambda^2 R^2} \right) I_{z=0} \quad (2.2)$$

This image intensity is  $[a^2/(\lambda R)]^2$  times stronger than the radiation intensity on the aperture plane. This amplification is named the Fresnel coefficient. The Fresnel coefficient indicates that larger aperture, shorter wavelength, and small, fast focal ratio produce a higher intensity image. The Strehl ratio of a practical system is given by the ratio of Equations (2.1) and (2.2).

After the first (piston) and second (tilt) aberration terms in a Taylor expression have been removed, the wavefront error becomes the difference between the practical wavefront and its best fit Gaussian one. The Strehl ratio is:

$$S = \frac{I(P)}{I_{\phi=0}(P_{r=0})} = \frac{1}{\pi^2} \left| \int_0^1 \int_0^{2\pi} e^{ik\phi_p} \rho d\rho d\theta \right|^2 \quad (2.3)$$

where  $\phi_p$  is wavefront deviation away from its best fit Gaussian wavefront. If  $\Phi^n$  represents the ensemble average of the  $n$ -th power of wavefront error  $\phi$ :

$$\Phi^n = \frac{\int_0^1 \int_0^{2\pi} \phi^n \rho d\rho d\theta}{\int_0^1 \int_0^{2\pi} \rho d\rho d\theta} = \frac{1}{\pi} \int_0^1 \int_0^{2\pi} \phi^n \rho d\rho d\theta \quad (2.4)$$

The wavefront error variance  $(\Delta\phi)^2$  is:

$$(\Delta\phi)^2 = \frac{\int_0^1 \int_0^{2\pi} (\phi - \Phi)^2 \rho d\rho d\theta}{\int_0^1 \int_0^{2\pi} \rho d\rho d\theta} = \Phi^2 - (\Phi)^2 \quad (2.5)$$

If the rms wavefront error is  $\Delta\phi < \lambda/2\pi$  and there is no correlation between errors in  $N$  sub-apertures ( $N$  is a large number), the corresponding Strehl ratio is:

$$S = 1 - \left( \frac{2\pi}{\lambda} \right)^2 (\Delta\phi)^2 \cong \exp \left[ - \left( \frac{2\pi}{\lambda} \right)^2 (\phi_p)^2 \right] \quad (2.6)$$

This equation is the same as Equation (1.119). The wavefront error discussed is a small and randomly distributed one with very small correlation lengths, it has no repeatable pattern, and has a continuous first derivative (slope). In this case, the image intensity loss is independent upon the wavefront error details. However, if the wavefront error is large, the formula has error. The reader may reference Section 7.1.2 for a better understanding of this formula.

Since the mirror surface error is half of the wavefront error, Equation (2.6) provides an important criterion for the mirror surface requirement of an optical telescope system. Table 2.1 lists relative image intensities for different wavefront errors. Usually, a relative image intensity of 67% is acceptable; the corresponding rms mirror surface error allowed is, therefore, 1/20th of the wavelength.

The image size of a ground-based astronomical optical telescope without adaptive optics is limited by the site atmospheric seeing. To achieve maximum

**Table 2.1.** The relationship between wavefront rms error and relative image intensity

$\Delta\phi$	$\lambda/10$	$\lambda/12$	$\lambda/14$	$\lambda/16$	$\lambda/18$	$\lambda/20$	$\lambda/22$	$\lambda/24$
$S$	0.674	0.760	0.817	0.857	0.885	0.906	0.921	0.933

telescope efficiency, 90% of image energy should be within the best seeing disk and 80% of the received energy should fall within a diameter of  $0.15''$  to  $0.30''$ ; for telescopes without adaptive optics. For telescopes in space or with adaptive optics, details of the Airy disk can be resolved. The mirror surface rms error should be smaller than  $1/40$ th of the wavelength. A target image accuracy of  $0.02''$  may be required. These tolerances are very stringent, so that the mirror manufacture and support are demanding for space optical telescopes. In some publications, the Fried parameter, which is related to FWHM of image size, is used as the error tolerance specification. A Fried number of 60 cm is equivalent to a FWHM of  $0.17$  arcsec (Hill, 1995).

### 2.1.2 Mirror Surface Error and Mirror Support Systems

Mirror surface error comes from three major sources: mirror manufacture, mirror support, and other influences. Mirror manufacture produces a fixed surface error from polishing and testing, the mirror support system produces an elevation dependent surface error, and other influences include actuator error and wind and thermal induced errors. The elevation dependent errors are from the gravity force which varies with the telescope pointing. Two typical gravity directions relative to the mirror are the axial and radial ones. To balance these gravity components, mirror supports on both directions are necessary. The design of these mirror supports are discussed in this section.

#### 2.1.2.1 Axial Support for Optical Mirrors

Mirror diameter-to-thickness ratio ( $d/t$ ), also known as aspect ratio, is very important in mirror support design. The smaller the aspect ratio is, the heavier the mirror and the higher the costs are. Classical mirrors have their aspect ratios between six and eight. These thick mirrors are easy to support. However, their thermal and gravitational inertias bring trouble to telescope designers. The first large thin mirror used is in the UK Infrared Telescope (UKIRT) built in 1973, with an aspect ratio of 16. Afterwards, thin mirrors with larger and larger aspect ratios were used in astronomy. As the mirror aspect ratio becomes large, the mirror support system design becomes critical. The surface deformation is also more sensitive to the support conditions.

Surface deformation of thin mirrors under an axial support system can be predicted by using classical thin plate theory. Under the thin plate assumption, the deformation of a plate is approximately a function of plate diameter and

thickness, being called the scaling law in the telescope mirror support design. The scaling law states that the rms surface deformation of a mirror is proportional to the fourth power of the diameter and is inversely proportional to the square of the thickness when the support conditions are not changed. With this scaling law, if the deformation of one mirror is known, then the deformations of other mirrors under a similar support condition can be accurately predicted.

From the scaling law, wavefront rms error curves are drawn in Figure 2.1 for mirrors of different diameter and aspect ratio under different support ring conditions (Cheng and Humphries, 1982). Four sets of wavefront rms error curves represent one-ring, two-ring, three-ring, and four-ring axial support systems, respectively. The figure shows that mirrors with an aspect ratio of 15 can be reasonably well supported by a one-ring axial support system up to a diameter of 1.25 m; by a two-ring support system up to 2.25 m; by a three-ring support system up to 4.5 m; and by a four-ring support system up to  $\sim 6$  m. The proportionality constants in these curves are derived from the data produced by the ESO CAT telescope, the 4 m KPNO telescope, the 3.8 m UKIRT, and from

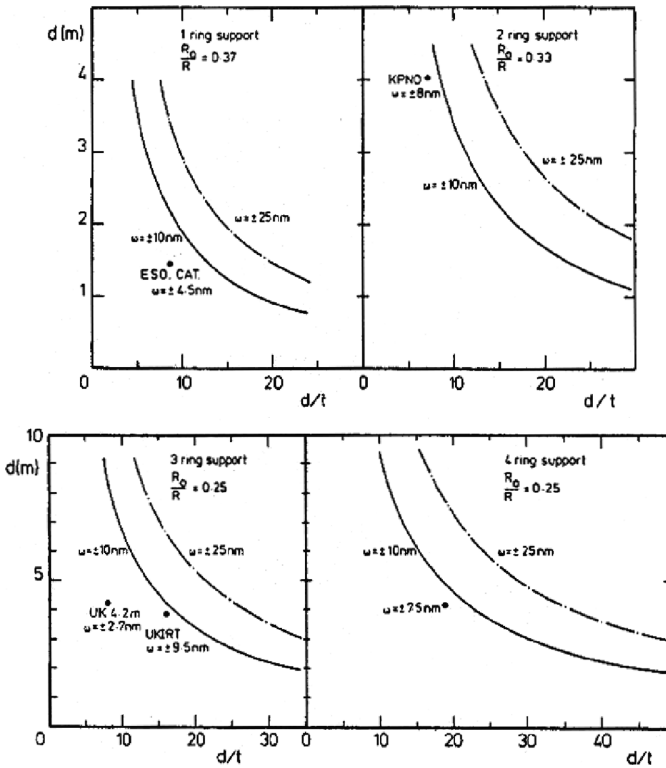


Fig. 2. 1. RMS wavefront errors for mirrors with different diameter and different aspect ratio on different rings of support system.

the finite element analysis (FEA). These curves can be used to estimate the surface rms errors for mirrors of different size and different aspect ratio. If the specification of a mirror is provided, the number of support rings required can be roughly predicted.

More accurately, the mechanical surface rms error, not wavefront rms error, of a thin plate under an axial support system is (Nelson et al., 1982):

$$\delta_{rms} = \xi \frac{q}{D} A^2 \quad (2.7)$$

where  $A$  is the plate area,  $q$  the areal density, and  $D$  the bending stiffness of the plate. The value of  $\xi$  reflects the support condition and is called the support efficiency. If there are  $N$  support points on a thin plate, then the average support efficiency of each point  $\gamma_N$  can be used in the expression of the rms surface error. The average support efficiency is:

$$\gamma_N = \xi N^2 \quad (2.8)$$

For a practical mirror support system, each support point may have its own support efficiency, resulting in a larger edge deformation as the edge support points may have lower support efficiency. The support efficiency of any point may be close to, but never reach an ideal value. This ideal value is the support efficiency when  $A \rightarrow \infty$  and  $N \rightarrow \infty$ .

When  $A \rightarrow \infty$  and  $N \rightarrow \infty$ , the plate deformation is determined by only two factors: the arrangement of the support points and the plate area related to each support point ( $A/N$ ). Under this assumption, the ideal support efficiency of each support point can be found for three basic support point arrangements, i.e., triangular grid, square grid, and hexagonal grid (Figure 2.2). The deformation of these three grid supports can be found analytically through linear superposition. Therefore, the average support efficiency of each point  $\gamma_\infty$  for these three cases can be derived. In terms of the rms surface error, these average support efficiencies are (Nelson et al., 1982):

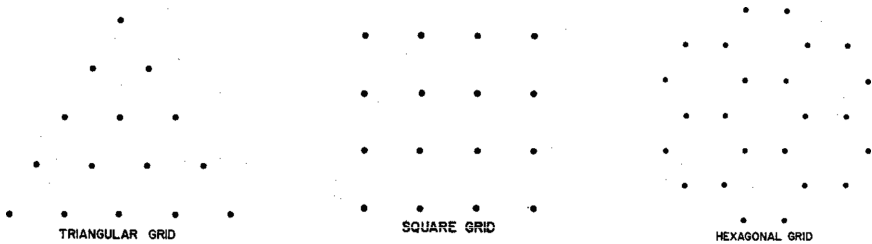


**Fig. 2.2.** Three basic grid arrangements: triangular, square, and hexagonal ones.

$$\begin{aligned}
\gamma_{triangular} &= 1.19 \times 10^{-3} \\
\gamma_{square} &= 1.33 \times 10^{-3} \\
\gamma_{hexagonal} &= 2.36 \times 10^{-3} \\
\delta_{rms} &= \gamma_i \frac{q}{D} \left( \frac{A}{N} \right)^2
\end{aligned} \tag{2.9}$$

The above efficiencies are independent of the Poisson ratio of the plate material. If the maximum, or the peak surface deformation, is considered, the average support efficiencies of these three cases are respectively  $4.95 \cdot 10^{-3}$ ,  $5.80 \cdot 10^{-3}$ , and  $9.70 \cdot 10^{-3}$ . The triangular grid has the highest support efficiency (or the lowest support efficiency number). This efficiency number can be set as a standard in the discussion of a thin mirror support system.

For circular thin plates on a multi-ring support system, the support points within a ring are at the same radius. The deformation of the plate is a superposition of deformations introduced by each support point. If the number of the support rings is  $n$  ( $i = 1, 2, \dots, n$ ), the number of the support points of each ring is  $k_i$ , the weighting factor of each support ring is  $\varepsilon_i$ , and the angle between adjacent points in a ring is  $\phi_i$ , then the surface rms deformation can be expressed as:

$$\delta_{rms}(r, \theta) = \sum_i^n \varepsilon_i \delta_i(k_i, \beta_i, r, \theta - \phi_i) \tag{2.10}$$

where  $\beta_i$  is relative support radius of ring  $i$ . By providing  $\delta_i$  in Equation (2.10), all the terms are added after the weighting factor  $\varepsilon_i$  being considered. In the calculation,  $\delta_i$  can be expressed in Zernike polynomial forms. If  $n$  is large, the calculation of  $\delta_{rms}$  and the optimization of the support radius  $\beta_i$  are generally difficult.

The simplest case involves one support ring with only two variables: the relative radius of the support and the number of support points. Figure 2.3 shows the relationship between the relative support radius and the rms surface error for a one-ring support system.

If one support point is used, optimization of the radius is not necessary. The support efficiency is  $\xi = \gamma_1 = 2.62 \cdot 10^{-3}$ . If two support points are used, optimization of the radius is necessary. At the optimum radius of about 0.35, the support efficiency is  $\xi = 2.16 \cdot 10^{-3}$  and the average support efficiency of each point is  $\gamma_2 = 2^2 \cdot \xi$ . The rms surface error decreases slightly. However, the support efficiency of each point decreases greatly. Figure 2.3 also shows the efficiencies for three, six, and more support points within one ring. When a continuous support ring is used, the optimum support radius is 0.683. The rms surface error is only 4% of that using an outer edge support. This efficiency increase demonstrates the importance of the mirror support system optimization.

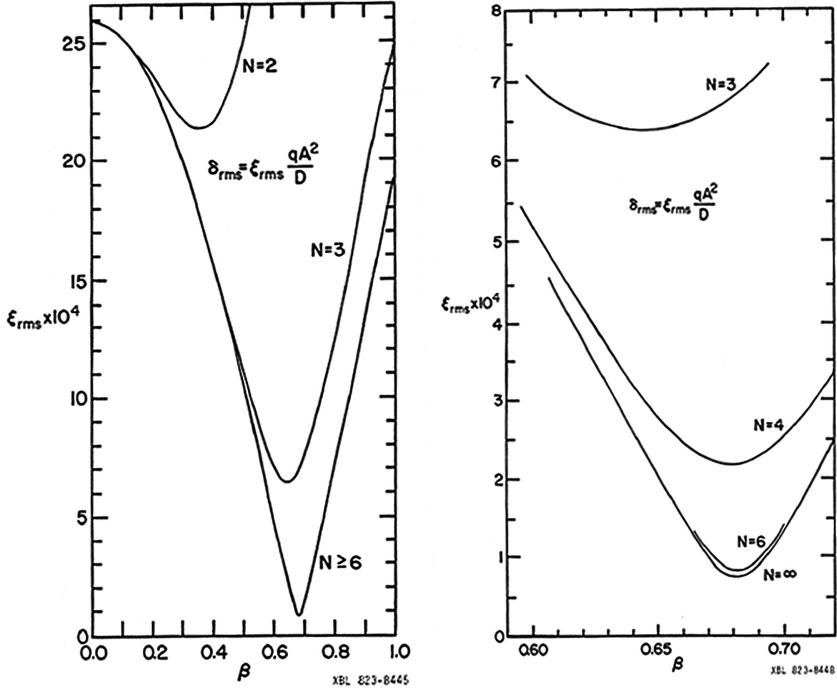


**Fig. 2.3.** RMS errors of the mirror surface as a function of relative support ring radius for different one ring support conditions and the figure on the right shows enlarged details (Nelson et al., 1982).

For two- or more-ring support systems, the plate surface deformation is also a function of Poisson ratio of the mirror material. Assuming the Poisson ratio is 0.25, by adding an additional point on the plate center in a six-point one-ring system, a seven-point two-ring support system is formed. After the radius optimization, the optimum arrangement has a support efficiency of  $\xi = 0.045 \cdot 10^{-3}$  and the average support efficiency of each point of  $\gamma_7 = 2.40 \cdot 10^{-3}$ . An eight-point two-ring system does not produce a satisfactory result and, thus, has never been used in practice. A nine-point two-ring system is the best among two-ring support systems. However, nine support points still can not form an integrated triangular arrangement. Under this support condition, the reduction of the rms surface error is still limited even compared with a seven-point two-ring support system. The average support efficiency of each point decreases greatly (Figure 2.4). A 12-point two-ring support system forms a real integrated triangular grid. Under this condition, both the rms surface error and the average support efficiency of each point are improved. The support efficiency is  $\xi = 0.013 \cdot 10^{-3}$  and the average support efficiency of each point is  $\gamma_{12} = 1.88 \cdot 10^{-3}$ . It is worth noting that  $\gamma_{12}$  is merely 1.6 times worse than  $\gamma_{triangular}$ .



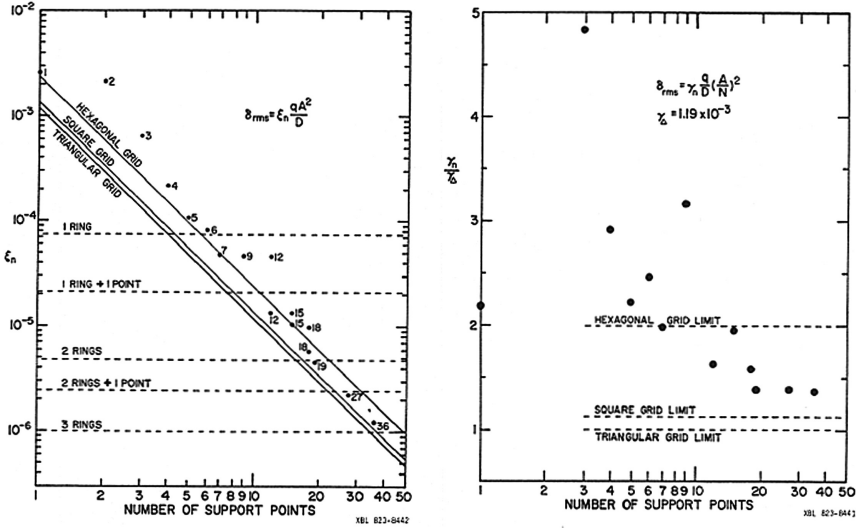


Fig. 2.4. The support efficiency as a function of the number of support points for different support systems (*left*) and the normalized efficiency of each point as a function of the number of support points (*right*) (Nelson et al., 1982).

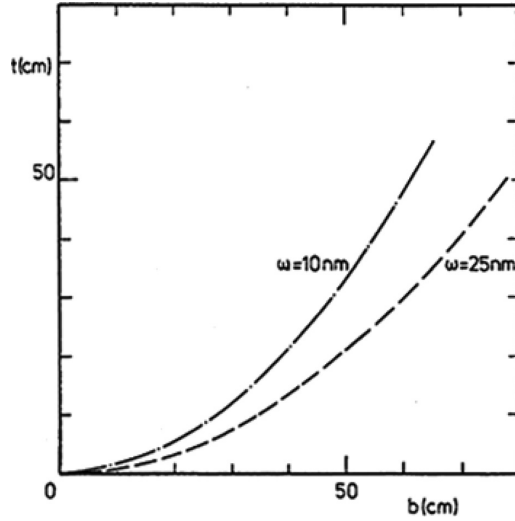
By adding more points, a 15-point two-ring system has an even better average support efficiency,  $\gamma_{15}$ . When an 18-point two-ring system is used, the support efficiency increases again. If an additional support point, the 19th, is added at the center of this system, the support efficiency  $\xi$  and the average support efficiency of each point  $\gamma_{19}$  decreases rapidly. As the support point number further increases, the support efficiency  $\xi$  goes down gradually and the efficiency of each point  $\gamma_N$  approaches  $\gamma_{triangular}$ . For example, the support efficiency of each point for an optimized 36-point system is  $\gamma_{36} = 1.4\gamma_{triangular}$ . However, too many support points produce many more variables in the system optimization. Therefore, careful calculation is necessary as a minute change of parameters can result in large variation of the surface rms error.

Figure 2.4 gives the ratio between the support efficiency of each point  $\gamma_N$  and the triangular grid efficiency  $\gamma_{triangular}$ . The overall support efficiency  $\xi$  is also included. All the data points in the figure are for optimum support systems.

For a large thin mirror, the support point number  $N$  is usually inversely proportional to the average support area. If the mirror thickness is  $t$ , then the following relationship exists:

$$\delta_{rms} \sim \frac{1}{(tN)^2} \quad (2.11)$$

For improving the surface accuracy, adding more support points or using a thick mirror are necessary. For the same surface accuracy, a thinner mirror



**Fig. 2.5.** The relationship between mirror thickness, support distance and the surface rms error.

requires more support points than a thicker one. More support points reduces the distance between each support point. If the most efficient triangle grid support is used and the mirror is of Cer-Vit material with  $E = 9.2 \times 10^{10} \text{ Nm}^{-2}$ ,  $\nu = 0.25$ , and  $\rho = 2,500 \text{ kg m}^{-3}$ , the relationship between the mirror thickness, the distance between support points, and the surface rms error is shown in Figure 2.5.

### 2.1.2.2 Radial Support for Optical Mirrors

The maximum mirror deformation caused by a radial (lateral) mirror support system occurs when the telescope points to horizon. At this position, the gravity and support forces are both perpendicular to the mirror surface (Figure 2.6). The major mirror deformation at this position is still along the axial direction  $z$ . The strain  $\varepsilon_z$  produced in the  $z$  direction is due to the Poisson effect of the support forces:

$$\varepsilon_z = -\frac{\nu}{E}(\sigma_x + \sigma_y) \quad (2.12)$$

where  $E$  is the Young modulus,  $\nu$  the Poisson ratio, and  $\sigma_x$  and  $\sigma_y$  the stresses in  $x$  and  $y$  directions, respectively. If the  $x$  direction is along the vertical line, the stress in this direction is caused by gravity and the radial supporting forces. The stress in the  $y$  direction is not related to gravity and is determined by the mirror support conditions.

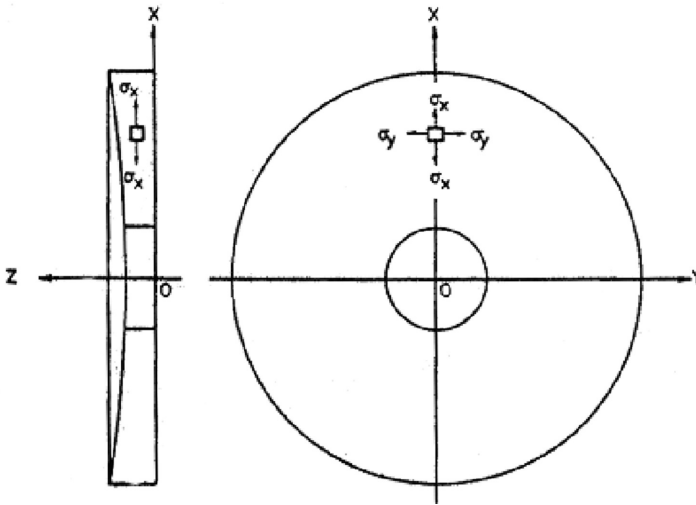


**Fig. 2.6.** Mirror stress distribution under the radial mirror support system (Cheng and Humphries, 1982).

Three radial mirror support systems exist and their force conditions are illustrated in Figure 2.7. Figure 2.7(a) shows the force condition when a mercury belt is used (a rubber torus filled with mercury and with a fixed inner contact area). Figure 2.7(b) shows the force condition for a cosine radial support system (counterweight and cantilever system in the radial direction). And Figure 2.7(c) shows the force condition of a vertical push-pull support system of which all supporting forces are parallel to the vertical axis (counterweight and cantilever

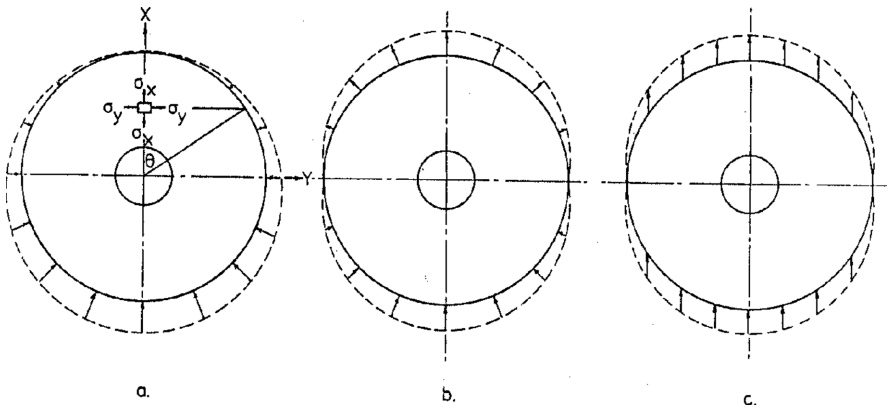


**Fig. 2.7.** Force conditions of (a) mercury belt radial support, (b) the cosine lateral force radial support, and (c) the vertical push-pull radial support (Cheng and Humphries, 1982).

system in the vertical direction). The stresses along the  $y$  direction of these three radial support systems are:

$$\begin{aligned}\sigma_{ya} &= -k_a(1 - \cos \theta) \sin \theta \\ \sigma_{yb} &= k_b \cos \theta \sin \theta \\ \sigma_{yc} &= 0\end{aligned}\tag{2.13}$$

where  $\theta$  is the polar angle in the mirror plane and  $k_a$  and  $k_b$  are positive constants. From the formulas, it is found that the stresses along the  $y$  direction in System (a) and in the bottom part of System (b) are of the same sign as stresses in the vertical direction. The contributions from these stresses to the surface error in the  $z$  direction are added to that from stresses in the vertical direction. Therefore, the minimum mirror surface deformation along the  $z$  axis happens only in System (c) where stresses in the  $y$  direction vanish.

If a paraboloidal mirror has a flat-back surface and is supported as in configuration (c), a small section of the mirror on the vertical symmetrical plane is shown as in Figure 2.8. Since the mirror thickness in the  $z$  direction is expressed as  $z = (x^2/(4F)) + t_0$ , where  $t_0$  is the thickness at the vertex and  $F$  the focal length, then the deformation caused by the Poisson effect is  $w = z \cdot \varepsilon_z$ , where  $\varepsilon_z$  is the strain in the  $z$  direction. The deformation of the mirror surface is:

$$w = \frac{\nu \rho g}{E} \left( \frac{R_0}{12fd} + R_0 t_0 \right) - \frac{\nu \rho g t_0}{E} \cdot x - \frac{\nu \rho g}{12Efd} \cdot x^3\tag{2.14}$$

where  $\rho$  is the material density,  $g$  the gravitational acceleration,  $R_0$  the radius of the central hole,  $t_0$  the thickness at the central hole,  $f$  the focal ratio, and  $d$  the mirror diameter. The first and second terms in this expression are constant and

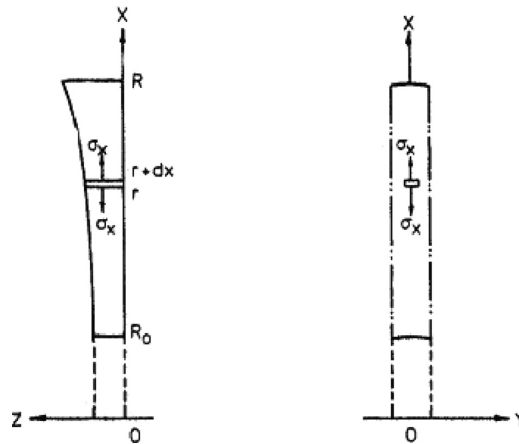


Fig. 2.8. Mirror stress under a vertical push-pull lateral support system.

linear terms, respectively. Neither of these have an influence on the surface rms error. Only the third term will cause astigmatism of the wavefront. This undesirable deformation has its maximum at a position of  $x = d/2$  and its value is:

$$w_{\max} = \frac{\nu \rho g}{96 E f} \cdot d^2 \quad (2.15)$$

If Cer-Vit material is used with the Young modulus of  $E = 9.2 \times 10^{10} \text{ N} \cdot \text{m}^{-2}$ , the Poisson ratio of  $\nu = 0.25$ , and the density of  $\rho = 2,500 \text{ kg m}^{-3}$ , then the relationship between the maximum surface error, the mirror diameter, and the f-ratio for a flat-back mirror under radial support system is shown in Figure 2.9. The maximum of the undesirable deformation caused by the Poisson effect is proportional to the diameter squared and is inversely proportional to the focal ratio. In general, this deformation is small in comparison with errors of the axial support case and will not produce serious effects on the telescope image. This is why the radial mirror support is less important than the axial one.

The depth of a curve is called sagitta. For a large parabolic mirror, the sagitta is  $S = d/(16f)$ . A large sagitta value of a flat-back mirror produces different thermal inertia along the radius, resulting in thermal-induced surface error. A meniscus mirror with uniform thickness avoids this thermal problem. The lateral support system for a meniscus mirror is slightly more complicated than that of a flat-back one. The main concern is that the lateral support forces have to pass through the mirror section center of gravity they support. The distance between combined support force and center of gravity produces a

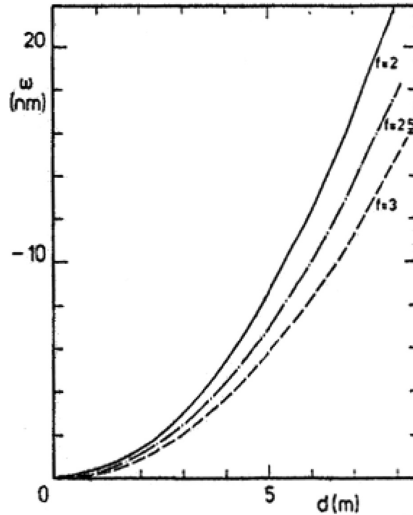


**Fig. 2.9.** Maximum flat-back mirror deformation under a push-pull lateral support system (Cheng and Humphries, 1982).

harmful bending moment which may produce large mirror surface deformations. The deformation caused by the Poisson effect is generally small and most of it varies linearly with the distance to the support point. However, deformations caused by bending moments are large and vary in a high power nonlinear fashion with the distance to the support point.

To reduce the deformation caused by the bending moment, the lateral support forces can be distributed inside small holes over the mirror back surface. In this way, the distance between the lateral support point and the local center of gravity of the mirror section is reduced. The combined lateral support force is on the same plane as the center of gravity of the mirror.

The bending moment caused by the lateral support of a meniscus mirror is proportional to both the diameter and thickness but inversely to the focal ratio. The deformation caused by this bending moment is proportional to the mirror area but inversely to the focal ratio and the square of the mirror thickness. Therefore, when the mirror aspect ratio increases, the mirror lateral support design becomes more important to the mirror surface deformation.

### 2.1.3 Surface Error Fitting and Slope Error Expression

An ideal Gaussian wavefront on an aperture plane is flat in shape. For any deformed wavefront, there exist many Gaussian reference wavefronts. However, only one among these has the minimum deviation from the deformed wavefront. This particular reference wavefront is the best fit wavefront. Relative to the original coordinate system, the best fit wavefront may have coordinate rotation, coordinate shift, and focal length change. The difference between the deformed and the best fit wavefronts is the wavefront error or the path length error. The wavefront error produced by a mirror is twice the mirror surface error. Wavefront error relative to the wavelength is called wavefront phase error. A wavefront error of half wavelength is equal to a wavefront phase error of  $180^\circ$ .

When an ideal telescope mirror, either paraboloid or hyperboloid in shape, is under gravity loading, the surface shape will change. For a deformed mirror surface, there is a best-fit reference surface. Detailed formulation of the best fit surface is provided in Section 7.1.4.

The best fit process for optical mirrors, where the f-ratio is large (comparing with a radio dish), is much easier. This is especially true when a multi-ring axial mirror support system is used. One convenient solution in the mirror support optimization is to consider only the axial coordinate shift. The principle is named equal softness. The ideal best fit surface of a mirror is a surface with an axial displacement from the original one. This simplification will reduce the workload in the mirror support optimization. The wavefront rms errors mentioned in the previous section were also obtained by using this simplified best fit method.

Apart from wavefront error, slope error is also used to describe the mirror deformation. The slope error is a measure of surface long-range modulations or

zones with ripple wavelengths (not optical wavelength) typically in the centimeter to tens of centimeter range. Because of the mirror slope error, the wavefront distortion is produced. The wavefront slope error is twice the mirror slope error. The slope error produces image blur size increase and resolution decrease. The resulting image blur size and resolution can be computed using geometrical optics. The slope angle is proportional to the image blur angle. The wavefront slope can be directly detected by a number of wavefront sensors, such as the Hartmann one. Maximum image diameter is about four-times the maximum mirror slope error, or twice the maximum wavefront slope error. However, limitation exists when the slope error instead of wavefront error is used for optical systems. If the wavefront or mirror surface ripple amplitude becomes so small relative to the wavelength (as may occur, for example, in going from visible to infrared) that the geometrical optics will be no longer valid then the effects of slope error may be greatly reduced.

Usually, the mirror slope error ( $S$ ) is proportional to the rms surface error and is inversely proportional to the effective mirror support distance ( $u$ ). The effective support distance is defined by the formula  $N\pi u^2 = A$ , where  $A$  is the mirror area and  $N$  the number of support points. Therefore, the mirror slope error can be expressed as (Nelson et al., 1982):

$$S = g_N \frac{q}{D} \left( \frac{A}{N} \right)^{3/2} \sim \frac{1}{t^2} \left( \frac{A}{N} \right)^{3/2} \quad (2.16)$$

where  $q$  is the areal density,  $D$  the diameter, and  $t$  the thickness. In this equation, the constant  $g_N$  can be obtained from the calculation and, in most cases, it can be expressed as a function of mirror support efficiency  $\gamma_N$ :

$$g_N = 9\gamma_N \quad (2.17)$$

## 2.2 Lightweight Primary Mirror Design

### 2.2.1 Significance of Lightweight Mirrors for Telescopes

The primary mirror is the most important component of an optical telescope. Its surface should maintain high accuracy under the telescope operating conditions. The weight and cost of the mirror are determining factors for the telescope total weight and total cost.

The mirror cell supports the primary mirror through a support system. Most support systems involve floating counterweight cantilever devices or air pads so that small changes in support position produce little effect on the mirror surface shape. However, any support system has a limited dynamic range. Therefore, the mirror cell has to be stiff enough so that its deformation does not exceed this dynamic range. The dimension and material density of traditional mirror cells

are usually larger than that of the mirror. Therefore, the weight of the cell is in the same magnitude of the mirror.

The telescope tube supports the primary mirror at one side and the secondary assembly at the other side. Therefore, the tube weight, including the center section, is related to the weight of both the mirror and cell. The weight of the mount structure is also related to the mirror weight directly or indirectly. Table 2.2 lists relative weights of all telescope components in a classical telescope relative to the primary mirror weight. From the table, one would find how important the mirror weight reduction is to the telescope weight.

The cost of any engineering project is always proportional to the structural weight. The cost–weight ratio is an indicator of the structure precision and complexity. As the mirror weight is a deciding factor on the overall telescope weight, therefore, the reduction of the mirror weight is very important in telescope design. To build an extremely large telescope with a nonstop increase of the aperture, the mirror weight reduction is a necessary first step.

In the past few decades, mirror weight reduction had been a major research topic for telescope scientists and engineers. A number of techniques developed in this aspect include: (a) using a thin mirror; (b) using a honeycomb mirror; (c) building a multiple-mirror telescope; (d) building a segmented mirror telescope (SMT); and (e) using mirrors made of metal, or carbon fiber reinforced plastic (CFRP) composite, or other special materials. These techniques are discussed in the following sections.

### 2.2.2 Thin Mirror Design

Cheng and Humphries (1982) and Nelson et al. (1982) pointed out that the surface error of any thin mirror may be reduced by an increase of the mirror support points and, in theory, a mirror can have a very large aspect ratio. Traditional telescope mirrors had their aspect ratios smaller than 10. Newly designed monolithic mirror telescopes have their mirror aspect ratios much larger than 20 and newly built segmented mirror telescopes have aspect ratios as large as 110. In an extreme case, the thin adaptive secondary mirror has an aspect ratio of 320.

**Table 2.2.** Weight ratios of major components for an optical telescope.

Name of component	Relative weight
Primary mirror	1.0
Primary mirror cell	1.5–3.3
Tube	3.5–10.0
Yoke	6.0–16.5
Mounting structure	6.0–20.0
Total	18.0–50.0



A key issue in the use of thin mirrors is the mirror support system. The factors which limit the increase of mirror aspect ratio are assembly and disassembly methods of the mirror, the maximum stresses during installation, the wind disturbances, and the resonant vibration.

The stresses of a primary mirror, except an extremely thin one, in normal working conditions are negligible. However, high stresses are induced during assembly and disassembly. The maximum stress  $\sigma_{\max}$  of a circular mirror during assembly is:

$$\sigma_{\max} = Kq \frac{d^2}{t} \quad (2.18)$$

where  $K$  is a constant determined by the mirror lifting condition,  $t$  the thickness,  $d$  the diameter, and  $q$  the density of the material. The condition of using this simplified formula is that the lifting force applied is on the middle plane of the mirror. When the lifting force is on the bottom of the mirror, this formula is still correct for the maximum stress estimation.

Traditional thick mirrors were lifted on the central holes. The lifting forces are applied on the bottom surface around the hole. If the mirror material has a density of  $q = 2,500 \text{ kg/m}^3$  and a Poisson ratio of  $\nu = 0.3$ , the relationship between the maximum stress, the diameter, and the aspect ratio during a central hole lifting is shown in Figure 2.10. In the figure, the maximum permissible stress for Cer-Vit material of about  $3 \times 10^6 \text{ N m}^{-2}$  is also plotted. From this figure,

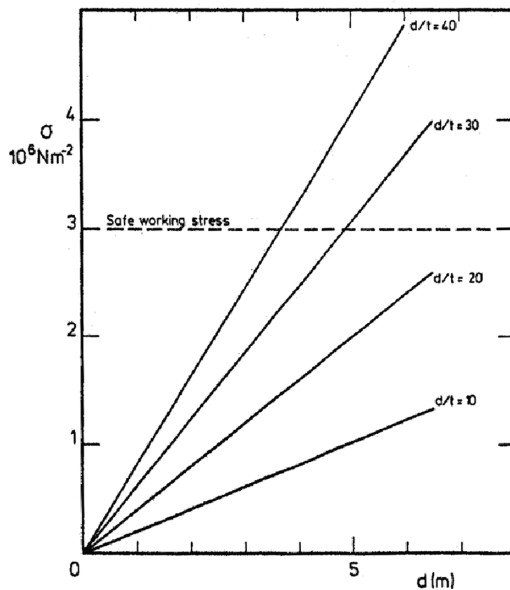


Fig. 2.10. The relationship between maximum stress, diameter, and aspect ratios.

mirrors of large aspect ratios using a central hole lifting may have unacceptable maximum stresses. The maximum stress in this case is in the tangential direction.

To reduce the stresses, the lifting position may move to the outer edge of a mirror. When the mirror is lifted on its outer edge, the maximum stress is still in the tangential direction. However, the maximum stress reduces to half of the numbers shown in Figure 2.11.

To further reduce the maximum stress during assembly, the lifting position should move to the middle radius of a mirror. If the lifting force is applied on a continuous circle with a radius of  $0.67 R$  ( $R$  is the radius of the mirror), the maximum stress is only one tenth of that when the lifting force is applied on the central hole. The maximum stress in this case changes from the tangential to the radial direction at the lifting radius. In Figure 2.11, stress distributions for different radius lifting are listed, where  $g$  represents the gravitational acceleration,  $\rho$  the density,  $\sigma_r$  the radial stress, and  $\sigma_t$  the tangential stress.

Normally, telescope mirrors use a single ring lifting. However, difficulties arise when the lifting radius is in the middle of sophisticated mirror support mechanisms. To solve the problem, a combination of the mirror cell and lifting

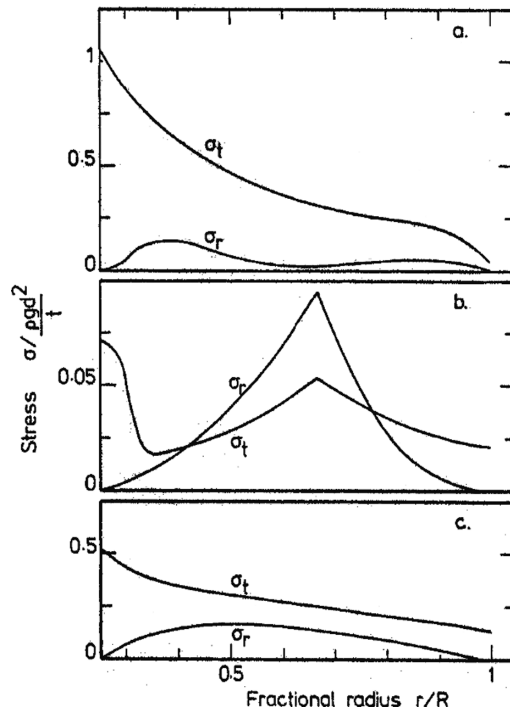


**Fig. 2.11.** Stress distribution under (a) a central ring support, (b) a 0.67-radius ring support, and (c) outer ring support (Cheng and Humphries, 1982).

mechanism is made during the assembly and disassembly processes. The mirror is lifted with its mirror cell, so the safety of the mirror is insured.

Another lifting method involves multiple vacuum lifting points on top of a mirror, which is often used in the mirror polishing process. Extremely thin mirrors can only be lifted with distributed multiple support point floating devices.

The wind disturbance on a mirror becomes serious as the mirror becomes very thin and is exposed to outside air flow. Mirror supports include floating ones, which do not take any additional loads, and positioning ones (hard points), which do take additional loads. Usually at least three positioning supports are used. If these positioning supports are evenly located on the outer radius of the mirror, the maximum deformation caused by a pressure load  $P$  is:

$$w_{\max} = 1.9 \times 10^{-3} \frac{\pi P d^4}{t^3} \quad (2.19)$$

This formula shows that the maximum deformation caused by wind is proportional to the cubic power of the aspect ratio. To increase the wind resistance of a mirror, the positioning support radius should be optimized. An optimized radius of the positioning supports has a normalized radius of 0.67. The maximum deformation in this case will reduce to a quarter of the above value. Further improvement in the wind resistance can be achieved by increasing the number of load bearing support (positioning) points or by using an adaptive optics mirror support system.

The natural frequency of a thin mirror can be expressed as:

$$\nu_R = \frac{2\phi \cdot t}{\pi \cdot d^2} \sqrt{\frac{E}{12(1-\nu)\rho}} \quad (2.20)$$

where  $\phi$  is a constant determined by the mode shape. If the hard points are arranged on the outer radius with a free edge, the value of  $\phi$  is 9.1. When Cer-Vit material is used, the natural frequency of a mirror is:

$$\nu_R = 1.14 \times 10^4 \frac{t}{d^2} (\text{Hz}) \quad (2.21)$$

where the unit of  $d$  and  $t$  is in meters. This formula shows that a 5 m mirror with an aspect ratio of  $d/t = 20$  has a natural frequency of about  $\nu_R = 100$  Hz. If the aspect ratio increases to 50, then the natural frequency would be reduced to 27 Hz. If three hard points are moved to 0.7 radius, the natural frequency will reduce by another factor of 4.

If the stiffness of the hard points is considered, the relationship with the frequency of the piston mode of a rigid mirror is approximately (Hill, 1995):

$$K_i = (2\pi v)^2 m / 3000 \quad (2.22)$$

where  $m$  is the mirror mass in kg,  $v$  the frequency, and  $K_i$  the stiffness of one hard point in N/mm. A small frequency number of the piston mode is undesirable. High stiffness of the hard points will minimize the wind and actuator error induced displacements and vibration amplitudes. To increase the natural frequency of the mirror system, it may be necessary to add more hard support points.

The friction of a mirror support system is another consideration when an aspect ratio is selected. The friction produces support force errors. A classical counterweight cantilever system usually has a friction coefficient of 0.1~0.3%. To ensure its optical performance, the aspect ratio of a mirror with this system should satisfy the following relationship:

$$d^2/t \leq 2500(cm) \quad (2.23)$$

For an air bag support system, the friction coefficient is about 0.01%. The corresponding number in the right hand side is 25,000 cm. Other factors, which restrict the use of very thin mirrors, include the mirror casting, mirror polishing, and mirror transportation. If we want to use an even larger aspect ratio, technology improvements in these fields are required.

### 2.2.3 Honeycomb Mirror Design

A honeycomb mirror is a sandwiched structure including face plate, honeycomb core, and base plate. The base plate may have holes for mirror supporting and ventilation. Honeycomb mirrors are light in weight, high in stiffness, and rigid in bending. The earlier applications of this type of mirror are the 4.5 m old Multi-Mirror Telescope (MMT) which was made of six 1.8 m honeycomb mirrors (note: The old MMT telescope was converted to a single mirror 6.5 m telescope in 1998) and the 2.4 m Hubble Space Telescope (HST). The largest honeycomb mirror has a diameter of 8.4 m.

Honeycomb mirrors are made by removing materials in the honeycomb holes or by fusing glass plates and core together at high temperatures. A rotational honeycomb mirror casting method was developed by the mirror laboratory of the University of Arizona for large honeycomb mirrors with a paraboloidal surface shape. The principle to form a paraboloidal shape when the glass is in a liquid form is the same as that of a rotational mercury mirror as discussed in Section 2.2.6. During the mirror casting process, the furnace is heated to 1,178 C and is rotating at a constant speed, few revolutions per minute, to shape the front mirror surface.

The rigidity of a honeycomb mirror is nearly equivalent to a solid one of a similar thickness, but with only a small fraction of the weight. The bending stiffness of a honeycomb mirror is approximately:

$$D = \frac{E(h+t)t^2}{2(1-\nu^2)} \quad (2.24)$$

where  $t$  is the thickness of the upper or bottom plates and  $h$  the thickness of the honeycomb core in the middle. The weight of a honeycomb mirror is  $(2t + \alpha h)/(2t + h)$ -times that of a solid one, where  $\alpha (\alpha \ll 1)$  is the relative density of the core compared with the face plate.

A honeycomb mirror also has lower thermal inertia than that of a solid one. The low thermal inertia reduces the temperature gradient within the mirror. If air ventilation is applied to the honeycomb cells, then normal borosilicate glass with a relatively larger coefficient of thermal expansion (CTE) can be used for large optical telescopes. The thermal time constant  $\tau$  of a plate is:

$$\tau = \frac{\rho \cdot c \cdot t^2}{\lambda} \quad (2.25)$$

For borosilicate glass, the density is  $\rho = 2,230 \text{ kg/m}^3$ , the specific heat  $c = 1,047 \text{ J/Kg } ^\circ\text{C}$ , the thermal conductivity  $\lambda = 1.13 \text{ W/m } ^\circ\text{C}$ , and  $t$  the thickness of the wall. The thermal time constant of a honeycomb mirror can be derived from its wall thickness. To further reduce its thermal time constant, ventilation may be added. Under air ventilation, the energy is conserved and the following formula exists (Hill, 1995):

$$m_g \dot{T}_g c_g = \dot{m}_a c_a (T_{exit} - T_{input}) \quad (2.26)$$

where subscripts  $g$  and  $a$  are for glass and air,  $T$  is the temperature,  $T_{exit}$  and  $T_{input}$  the exit and input air temperature. The specific heat of the air  $c_a$  is  $711 \text{ J/Kg } ^\circ\text{C}$  and the thermal time constant is related to air flow rate as:

$$\dot{m}_a = \frac{m_g c_g}{\tau \cdot c_a \eta} \quad (2.27)$$

where  $\eta = 0.7$  is the heat transfer coefficient (heat coupling coefficient) of the forced convection and  $\tau$  the thermal time constant.

The size of the honeycomb hexagonal cells is determined from the maximum deformation of the mirror face plate during polishing. For a given pressure loading, the deformation of the center point of a honeycomb structure is:

$$w = 0.00111 \frac{qb^4}{D} \quad (2.28)$$

where  $q$  is pressure loading,  $b$  the distance between two opposite sides of the cell, and  $D$  the bending stiffness of the face plate. If the average pressure during the polishing is  $q = 0.084 \text{ N/cm}^2$ , the top plate thickness is  $2 \text{ cm}$ , and the maximum

deformation allowed is  $1/20$ th of the visible wavelength, then the size  $b$  of the cell can be calculated. The thickness of honeycomb side wall is determined by the mirror's global surface deformation and is usually a quarter of the top plate thickness. With ventilation holes on the mirror back, the installation of the mirror support system is easy. A honeycomb mirror requires no special designed support devices. Figure 2.12 shows the axial and lateral support systems of a honeycomb mirror.

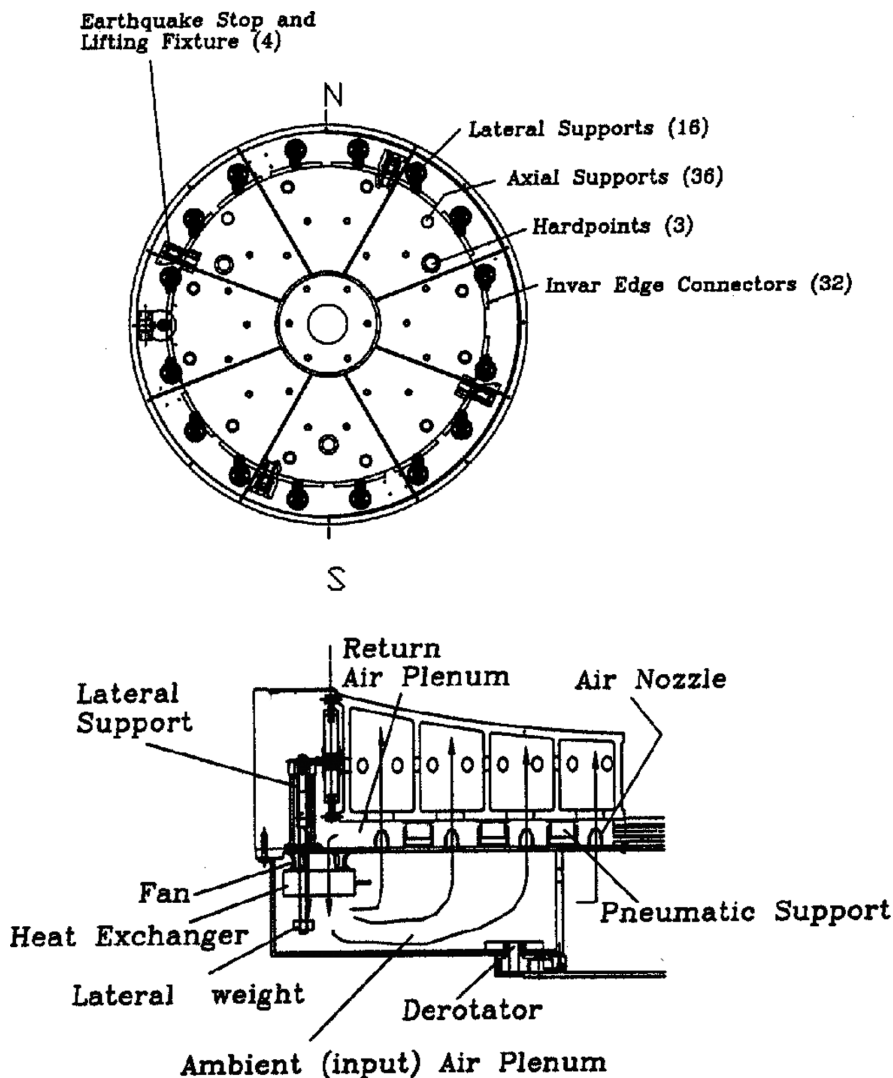


Fig. 2.12. An 8 m honeycomb mirror and its support system (West et al., 1997).

### 2.2.4 Multi-Mirror Telescopes

The name multi-mirror telescope comes from the old Multi-Mirror Telescope (MMT) which was built in 1979 with an equivalent aperture size of 4.5 m. This telescope had six independent tubes (or sub-telescopes) each with an aperture size of 1.8 m but firmly connected together by a large elevation (or tube) structure as shown in Figure 2.13. This design provided a new way to reduce the weight of a primary mirror.

Since the aperture area of an individual telescope tube accounts for only  $1/n$  of that of the whole telescope, where  $n$  is the number of sub-tubes used, so the aspect ratio of the mirror is equivalent to  $n^{1/2}$  of that of a monolithic primary mirror. Other advantages for a MMT telescope design are short tube length and large lateral tube dimension, so that the tube is stiff and the required dome is small.

For spectroscopic observation, when the co-focusing condition is met, the six sub-telescope foci are so arranged that they form a straight line on the entrance slit of the spectroscope. This avoids energy loss which happens in single aperture telescopes used in spectroscopic mode without an image slicer. Therefore, in this mode, the MMT works as one telescope.

Another intentional operation of this old MMT telescope was that the radiation collected by each sub-telescope was directed to a common focus in co-phasing condition, thus forming a Fizeau interferometer with a much larger baseline. However, the tube structure made of steel to support both the primary and secondary mirrors had serious uncorrectable thermal distortions and the telescope was lacking in optical path length equalization devices or optical delay lines to compensate these random phase differences. The wavefront co-phasing was nearly impossible. The field of view on its common focus was also limited due to a small angle between beams from all sub-telescopes in the common image plane. All these are reasons leading to the failure in this interferometer mode although some fringes were obtained occasionally. After 19 years of continuous struggle with the spectroscopic and independent small telescope observations, a conversion of the old MMT into a new 6.5 m single mirror telescope was finally made in 1998.

The old MMT was gone, but the idea to build a MMT-type Fizeau interferometer (Section 4.2.3) remains. For a coherent diffraction limited common focus image, all the sub-telescopes are required both co-phasing each other through sophisticated optical delay lines and free from atmospheric turbulence through adaptive optics. In the past, the technologies required to fulfill these two tasks were not ready, but now they are within reach.

A newly built MMT-type telescope is the Large Binocular Telescope (LBT) with two 8.4 m mirrors completed in 2008. With a separation between two mirror centers of 14.4 m, its common massive elevation structure is on hydrostatic pads to reduce the structural deformation. Now both sub-telescopes are in perfect working condition and used as an independent telescope, but the final target of this telescope as a Fizeau interferometer instrument has still not been realized.

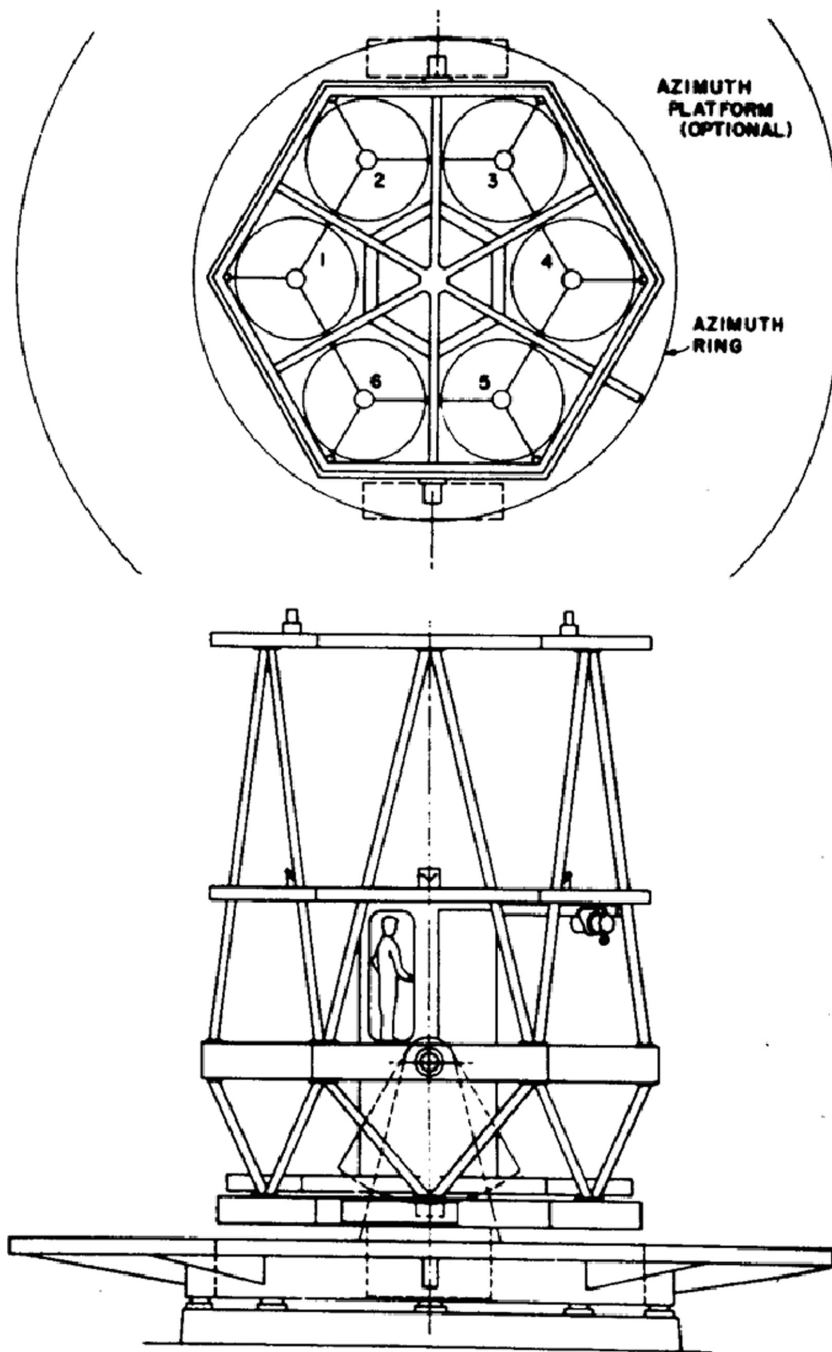


Fig. 2.13. The arrangement of the old MMT telescope.



### 2.2.5 Segmented Mirror Telescopes

The Segmented Mirror Telescope (SMT) represents a new approach to obtain a light weight primary mirror for extremely large optical telescopes. The extremely large optical telescopes are telescopes with their diameter far beyond 10 meters. Compared with the MMT design, the SMT, with all segments of the primary mirror reflecting light to a common secondary mirror can have both a large field of view and co-phase interferences between individual segments. The advantages of the SMT design include great mirror weight reduction, large cost savings, easy mirror handling and transportation, and small dome size.

A SMT telescope consists of many mirror segments, making up a larger light collecting area. Each of the 10 m Keck I and II telescopes has 36 1.8 m hexagonal mirror segments with a thickness of only 8.7 cm (Figure 2.14). Since the deformation of a thin mirror is proportional to the fourth power of diameter, the mirror support systems for smaller segments are much simpler in comparison with that for a monolithic larger primary mirror. The smaller segment diameter and repeatable segment patterns also lower the mirror manufacture, mirror polishing, and mirror transportation cost.

Two surface shapes are used for the SMT telescopes: a spherical one as used in the HHT and SALT telescopes and paraboloidal one as used in the Keck and Gran Telescopio Canarias (GTC). The GTC was built by Spain, Mexico, and University of Florida. The proposed TMT, GMT, and E-ELT will have a paraboloidal surface shape and the OWL a spherical surface shape.

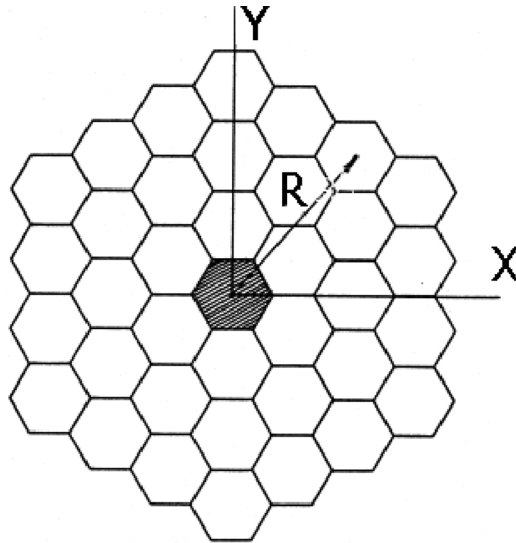


Fig. 2.14. The primary mirror of the 10 m Keck telescope.

With a spherical surface shape, the mirror segments are all identical, so that the mirror manufacture is easy and the cost is low. However, a complicated field corrector is needed to correct the spherical aberration although the field of view is wider. In general, the spherical primary mirror shape limits the usage of the telescope, so most telescopes use a paraboloidal surface shape.

With a paraboloidal surface shape, the system optical design is easier, but with a relatively smaller field of view. However, the mirror segments are different between rings. All these segments have off-axis paraboloidal surface shape, bringing difficulties in segment manufacture and polishing. The SMT telescopes require an accurate position control of each mirror segment to achieve a smooth coherent mirror surface. The strategy of the mirror segment position control is discussed in Section 4.1.4. In this section, the off-axis paraboloidal mirror segment manufacture is discussed.

The formulae for an axial symmetrical, conic surface are (Nelson et al., 1985):

$$\begin{aligned}
 Z(X, Y) &= \frac{1}{K+1} \left[ k - [k^2 - (K+1)(X^2 + Y^2)]^{1/2} \right] \\
 Z(X, Y) &= \frac{1}{2k}(X^2 + Y^2) + \frac{1+K}{8k^3}(X^2 + Y^2)^2 \\
 &\quad + \frac{(1+K)^2}{16k^5}(X^2 + Y^2)^3 + \frac{5(1+K)^3}{128k^7}(X^2 + Y^2)^4 \dots
 \end{aligned} \tag{2.29}$$

where  $k$  is the radius of curvature at the vertex,  $K$  the conic constant,  $Z$  the coordinate along the axis, and  $O$  the vertex of the surface. When the global coordinate system is replaced by a local one of  $p(x, y, z)$  (Figure 2.15), the conic surface can be expressed as a trigonometric series:

$$z = \sum_{ij} \alpha_{ij} \rho^i \cos j\theta \quad (i \geq j \geq 0, i - j = \text{even}) \tag{2.30}$$

In this expression, the first few coefficients are listed as:

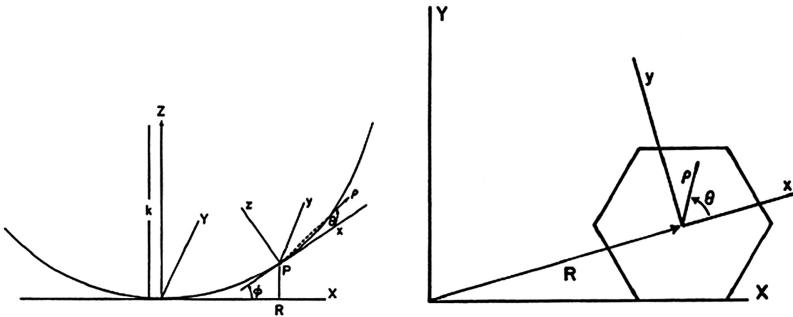


**Fig. 2.15.** The global and local coordinate systems for an off-axis, conic segment surface (Nelson et al., 1985).

$$\begin{aligned}
\alpha_{20} &= \frac{a^2}{k} \left[ \frac{2 - K\varepsilon^2}{4(1 - K\varepsilon^2)^{3/2}} \right] (\text{focus}) \\
\alpha_{22} &= \frac{a^2}{k} \left[ \frac{K\varepsilon^2}{4(1 - K\varepsilon^2)^{3/2}} \right] (\text{astigmatism}) \\
\alpha_{31} &= \frac{a^3}{k^2} \left[ \frac{K\varepsilon[1 - (K+1)\varepsilon^2]^{1/2}(4 - K\varepsilon^2)}{8(1 - K\varepsilon^2)^3} \right] (\text{coma}) \\
\alpha_{33} &= \frac{a^3}{k^2} \left[ \frac{K^2\varepsilon^3[1 - (K+1)\varepsilon^2]^{1/2}}{8(1 - K\varepsilon^2)^3} \right] \\
\alpha_{40} &= \frac{a^4}{k^3} \left[ \frac{8(1+K) - 24K\varepsilon^2 + 3K^2\varepsilon^4(1-3K) - K^3\varepsilon^6(2-K)}{64(1 - K\varepsilon^2)^{9/2}} \right] \\
&(\text{spherical aberration}) \\
\alpha_{42} &= \frac{a^4}{k^3} \left[ \frac{K\varepsilon^2[2(1+3K) - (9+7K)K\varepsilon^2 + (2+K)K^2\varepsilon^4]}{64(1 - K\varepsilon^2)^{9/2}} \right] \\
\alpha_{44} &= \frac{a^4}{k^3} \left[ \frac{K\varepsilon^2[1+5K - K\varepsilon^2(6+5K)]}{64(1 - K\varepsilon^2)^{9/2}} \right]
\end{aligned} \tag{2.31}$$

where  $a$  is the projected radius of a hexagonal mirror segment,  $\rho = (x^2 + y^2)^{1/2}/a$ ,  $\theta = \tan^{-1}(y/x)$ , and  $\varepsilon = R/k$ . The other coefficients are expressed in a generalized form as:

$$\alpha_{ij} \approx a^i \varepsilon^j / k^{i-1} \tag{2.32}$$

When  $i > 4$ , these coefficients are very small for a hexagonal mirror segment and can be neglected. The off-axis conic surface described in the above expression can be transformed into a symmetrical spherical surface by applying elastic deformations.

For a spherical surface,  $K$  equals zero and it leaves only two coefficients of  $\alpha_{20}$  and  $\alpha_{40}$  in the segment surface expression. The values of these two coefficients are  $a^2/(2k)$  and  $a^4/(8k^3)$ , respectively. By comparing the above off-axis conic shape with a best-fit spherical shape, the required elastic deformations for the surface shape transformation can be derived. The required deformations, which equal the differences between these two surface expressions, are (Lubliner and Nelson 1980):

$$\begin{aligned}
w &= \sum_{ij} a_{ij} \rho^i \cos j\theta \\
w &\cong \alpha_{20} \rho^2 + \alpha_{22} \rho^2 \cos 2\theta + \alpha_{31} \rho^3 \cos \theta + \\
&\quad \alpha_{33} \rho^3 \cos 3\theta + \alpha_{40} \rho^4 + \alpha_{42} \rho^4 \cos 2\theta
\end{aligned} \tag{2.33}$$

With classical thin plate theory, the required deformations are obtained by applying forces, moments, and distributed surface loads on the segment. These forces, moments, and distributed loads are also expressed in sine and cosine series as:

$$\begin{aligned}
 M(\theta) &= M_0 + \sum_n (M_n \cos n\theta + \bar{M}_n \cos n\theta) \\
 V(\theta) &= V_0 + \sum_n (V_n \cos n\theta + \bar{V}_n \cos n\theta) \\
 q(r, \theta) &= q_0 + q_1 r \cos n\theta + q_2 r \sin \theta \\
 V_0 &= -q_0/2 \\
 M_1 + aV_1 &= -q_1 a^3/4 \\
 \bar{M}_1 + a\bar{V}_1 &= -q_2 a^3/4
 \end{aligned} \tag{2.34}$$

The coefficients used in the above expressions derived from the plate deformation formulae are:

$$\begin{aligned}
 M_0 &= \frac{D}{a^2} [(2 + \nu)\alpha_{20} + 4(3 + \nu)\alpha_{40}] \\
 V_0 &= -\frac{D}{a^3} (32\alpha_{40}) \\
 M_1 &= \frac{D}{a^2} [2(3 + \nu)\alpha_{31} + 4(5 + \nu)\alpha_{51}] \\
 V_1 &= -\frac{D}{a^3} [2(3 + \nu)\alpha_{31} + 4(17 + \nu)\alpha_{51}] \\
 M_n &= \frac{D}{a^2} [(1 - \nu)n(n - 1)\alpha_{nm} + (n + 1)[n + 2 - \nu(n - 2)]\alpha_{n+2,n}] \\
 V_n &= \frac{D}{a^3} [(1 - \nu)n^2(n - 1)\alpha_{nm} + (n + 1)(n - 4 - \nu n)\alpha_{n+2,n}] \\
 q_0 &= 64D\alpha_{40}/a^4 \\
 q_1 &= 192D\alpha_{51}/a^5 \\
 q_2 &= 192D\beta_{51}/a^5
 \end{aligned} \tag{2.35}$$

where  $D$  is the plate bending stiffness and  $\nu$  the Poisson ratio. If a sine component exists in the deformation formula, then a sine term in shearing force, or moment, or distributed load expression is necessary. After applying these required loads, the problem of off-axis paraboloidal surface manufacture turns into simple spherical surface manufacture. The only difference is that shearing

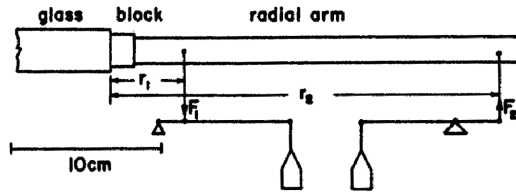


**Fig. 2.16.** The methods for applying shear force and bending moment during the off-axis mirror segment manufacture.

forces, or moments, or distributed loads have to be applied on the mirror segment during the segment polishing process.

Figure 2.16 shows a method of applying shearing forces and moments around a segment edge. The distributed loads can be provided in the axial mirror support system. Since the mirror segment is polished under internal stresses, this mirror manufacturing method is called “stressed polishing.” If a mirror segment under stress has been fabricated into a spherical shape, an off-axis paraboloidal shape can be obtained by releasing all the applied loads. Using this stressed polishing method, an ideal off-axis paraboloidal shape can be achieved step-by-step.

### 2.2.6 Metal and Lightweight Mirrors

Traditional mirror materials include glass ceramic materials, fused quartz, and other glasses. Nontraditional mirror materials include metals, metal alloys, SiC, and CFRP composites. The main motivation of using nontraditional materials is to reduce the weight and cost. Mirror material properties are discussed in next section. Liquid mirrors can also be formed by rotating liquid mercury inside flat dishes.

Metals or their alloys were used as optical mirror materials in the early days of mirror manufacture. They were replaced by glasses at the beginning of the 20th century because glasses have high surface smoothness and lower thermal expansion coefficients. Recent attempts at using metal mirrors include two Italian test optical telescopes: one is a 1.5 m one and the other is a 1.4 m one. The thermal sensitivity of a metal mirror is lower than that of a borosilicate (BSC) glass one as metals have high thermal conductivities. High thermal conductivity reduces temperature gradient inside a mirror. However, large metal thermal expansion produces large surface deformation.

Suitable metal mirror materials are aluminum, steel, titanium, beryllium and their alloys. The hardness of aluminum is low, so a coating of phosphor nickel alloy is used. The coated surface can be polished to required smoothness as used in a number of test optical telescopes. Steel and stainless steel are good metal mirror materials. Stainless steel with a hard alloy surface coating can be polished to optical surface quality. Beryllium and titanium mirrors have both

been used in space infrared telescopes. Beryllium is the mirror material of the James Webb Space Telescope (JWST) primary mirror as discussed in Section 5.3.2.

In general, metal mirrors are built by casting. However, a promising technique for large diameter mirrors is through micro-welding. The main obstacle of using metal mirrors in optical telescopes is the long-term shape warping. Many reasons produce warping of a metal mirror. Among these, the mirror's shape and thermal treatment are major ones. Asymmetrical mirror shape can produce larger warping, so that a feasible metal mirror shape is a meniscus of uniform thickness. The Italian 1.4 m aluminum mirror had a warping of one wavelength per ten years. Metal mirrors are easiest to build and the lowest in cost. If active optics is applied, metal mirrors may be used as candidates for future extremely large telescope mirrors.

Carbon Fiber Reinforced Plastics (CFRP) composite is another material for optical mirrors. The CFRP replica technique is a new achievement in the mirror manufacturing field. After 20-years practice, the CFRP replicated mirrors have been used in millimeter wavelength, infrared, optical, and X-ray telescopes. The great advantages of a CFRP mirror are light weight, high surface accuracy, high thermal stability, high surface smoothness, and low manufacture cost. The areal density of a CFRP mirror can be only a few kilograms per square meter.

To achieve a highly accurate mirror surface, a high precision mold is essential. A major problem in CFRP replication is the volume contraction of the resin material during the solidification process. The resin contraction is large and it produces mirror surface deformations. Therefore, it is necessary to reduce the resin contents in the CFRP mirror body. Other problems of the replication are air bubbles and the print-through of the ribs or fibers which overlap each other in the mirror surface. Air and water exist inside the resin in liquid form. During the solidification, water and air can turn into bubbles as temperature increases. Surface print-through is caused by the residual stress during the solidification process. The stress caused by overlapping of fibers in the mirror body may release and the fine print-through will appear on the mirror surface. All these reduce the smoothness and accuracy of the mirror. Without internal stresses, the surface smoothness of a CFRP replication mirror can be better than that of the mold surface used in the replication.

If a CFRP mirror's diameter is small, the mirror could be made by several symmetric layers of uni-directional fibers to form a meniscus shape. If the diameter mirror is large, a sandwiched structure should be used to guarantee the shape's stability. The sandwiched structure includes a top and bottom layer, both are curved in shape and a middle spacing part which can be formed from a number of CFRP short tubes with strictly the same length. The curing of CFRP parts should be done at a relatively low temperature. High temperature produces higher residual stresses. After the replication, the sandwich mirror is removed from the mold. The symmetry of fiber layers of each CFRP part should also be maintained to assure the mirror's long term stability.

Different carbon fibers have different thermal expansion coefficients (Section 8.3.1). For optical mirrors, low thermal expansion carbon fibers are preferred. Replication technology for a CFRP mirror depends largely on the mold's precision, workmanship, and proficiency of the technique. There are no unconquerable difficulties in the process. The replication technology can also be used in the manufacturing of deformable mirrors used in active or adaptive optics (Section 4.1.3).

Another CFRP replication method is to build a carbon fiber mirror blank and metal film on a mold surface first. The metal film is produced through electrical forming. The next step is to glue the metal film to the CFRP mirror blank using a thin layer of epoxy resin. This method is mainly used for mirrors of smaller aperture size.

Recently, silicon carbide (SiC) has been used as one optical or infrared mirror material (Section 9.1.3). A silicon carbide molecule is like diamond with half of the carbon atoms replaced by silicon atoms. SiC is an abrasive material. However, sintering (hot pressing), chemical vapor deposition (CVD), and reaction bonding lead to silicon carbide mirror blanks. One of these approaches is to obtain a soft blank through iso-static pressing of pure silicone carbide powder. The soft blank called "green-body" is workable to produce shape change. After milling the blank into its final geometry, the substrate is sintered at 2,000°C. The hardened segment is finally grounded and polished.

In CVD approach, gaseous chemicals react on a heated surface (often graphite) to form solid crystalline material. The process is slow, but it will produce a 100% dense, pure compound. This method can also produce a mirror surface with an integrated rib structure. However, the hardness of the compound makes mirror figuring and polishing time-consuming and difficult. In silicone carbide mirror polishing, diamond powder is the only abrasive used.

The reaction bonding is a cast and chemical process. First, high-grade silicone carbide is manufactured by chemical leaching to purify the base SiC abrasive. Leaching is a process of extracting a substance from a solid by dissolving it in a liquid. Then the powder is molded as the SiC is suspended in a silica-based gel. The substrate is heated to 950°C to remove the inert materials through evaporation. Small mirror blanks can be assembled to form a large mirror blank in this stage. Next, the substrate is heated again to 1,550°C in the presence of methane gas in vacuum. The carbonized substrate is immersed in molten silicon which fills the voids. This process produces a substrate of 83% SiC and it can be polished to a smoothness of 10 Å.

In this section, it is worth mentioning the rotational mercury mirror experiment. One project is the 6 m diameter Large Zenith Telescope (LZT) east of Vancouver, Canada. The project was developed from a 2.7 m one. This telescope mirror is a large plate filled with mercury, rotating at a constant rate over a precision air bearing. The plate container has a roughly parabolic shape to reduce the mass of mercury. The thickness of the mercury is only 1 mm.

The mercury has a relatively high reflectivity ( $\sim 80\%$ ). The rotating speed of the plate  $\omega$  is directly related to the focal length  $F = g/(2\omega^2)$ , where  $g$  is the

Table 2.3. Thermal and structural properties of some mirror materials

	Al	Steel	Invar	BSC glass	Fused silica	Cer-Vit	CFRP	SiC	Titanium
$\alpha[K^{-1}]$ CTE	$23 \times 10^{-6}$	$11 \times$	$1 \times$	$3.2 \times$	$0.05 \times$	$0.05 \times$	$0.2 \times$	$2 \times$	$12 \times$
$\lambda[W/mK]$	227	251	10	1.13	1.31	1.61	10	150	21.9
conductivity									
$c[J/kgK]$	879	502	500	1047	770	821	712	670	523
capacity									
$\rho[kg/m^3]$	2700	7750	8130	2230	2200	2530	1800	3140	4650
density									
$\delta = \lambda/c\rho$	$95 \times 10^{-6}$	$6.5 \times$	$2.5 \times$	$.48 \times$	$.77 \times$	$.79 \times$	$7.8 \times$	$.86 \times$	$9.0 \times$
$\delta/\alpha$	4.16	0.59	2.46	0.15	15.4	15.8	39.0	0.43	0.75
$E[N/m^2]$	$72 \times 10^9$	$210 \times$	$145 \times$	$68 \times$	$66 \times$	$91 \times$	$105 \times$	$430 \times$	$100 \times$
modulus									
$\nu$ Poisson	0.34	0.28	0.30	0.20	0.17	0.24	0.32	0.15	0.36
$E/\rho g(1 - \nu^2)$	$307 \times 10^4$	$299 \times$	$199 \times$	$322 \times$	$315 \times$	$389 \times$	$662 \times$	$1726 \times$	$252 \times$

Note:  $\delta = \lambda/c\rho$  is thermal sensitivity and  $E/\rho g(1 - \nu^2)$  is bending stiffness. BSC glass is borosilicate glass.



acceleration of gravity (for a 6 m mirror, the speed of rotation is 8.5 s/revolution). However, this type of mirror also has drawbacks: (a) its location has to be far away from any vibration source. (b) The rotating speed has to be smooth and uniform. (c) The mirror can only be used in zenith position. If star tracking is required, the optical device at the focus is complicated. (d) Because of the low viscosity of mercury, the aperture size is limited. And (e) there is vaporization of mercury, contamination from sulfur and phosphate in air, and surface ripples caused by a gentle breeze. The last issue may be solved by clamping a thin stretched film of Malar over the top of the mirror surface.

At present, a Large Aperture Mirror Array (LAMA) with 66 individual 6.15 m mercury mirror telescopes is planned and another large mercury mirror on the pole area of the moon is proposed for astronomy.

Table 2.3 lists thermal and mechanical properties of some common mirror materials. Some special details of the mirror materials will be discussed in the next section.

## 2.3 Mirror Polishing and Mirror Supporting

### 2.3.1 Material Properties of Optical Mirrors

Mirror materials should have special properties in order to maintain a stable, high-precision surface shape. Ceramic materials, such as Cer-Vit, Zerodur, and fused quartz are major optical mirror materials. New mirror materials include CFRP, SiC, metals, and alloys.

What are the basic requirements of optical mirror materials? First, the material should have excellent shape stability so that the mirror can maintain its high precision shape over a very long period. Second, the CTE of the material should be close to zero so that the shape of the mirror will not change when temperature changes. Third, the material should have enough rigidity and hardness to sustain stresses induced during fabrication and transportation. And fourth, the material surface should be smooth after polishing and capable of being coated with a thin reflective metal film in a vacuum condition. Some soft materials, which cannot be polished, can also be used by coating a layer of hard material on their surfaces.

Mirror material selection is a tradeoff process. Many factors influence the material selection. These include mechanical and thermal properties, material availability, cost, weight, transportation, fabrication, and others. Space optical telescopes require light weight materials.

Surface smoothness, or roughness, is one important mechanical property for mirror material. Surface roughness is defined as surface height rms error in an extremely high spatial frequency (small scale) range. The roughness measurement of the optical surface requires an extremely high spatial frequency of 100–200  $\mu\text{m}^{-1}$ . The surface roughness directly influences light scattering on the

surface. In the optical region, the total integrated scattering (TIS) is a function of surface roughness:

$$TIS = \left( \frac{4\pi\sigma}{\lambda} \right)^2 \quad (2.36)$$

where  $\sigma$  is the roughness and  $\lambda$  the wavelength. Since the TIS is inversely proportional to the square of the wavelength, mirrors used in optical and ultraviolet regimes require a very small surface roughness number (Figure 2.17).

Surface roughness is related to mirror material and mirror fabrication. Glass materials of fused silica or borosilicate glass have a surface roughness of 8 Å (Angstroms =  $10^{-10}$  m) after fine polishing. After normal polishing the roughness achieved is of 25 Å. Stainless steel can reach a roughness of 40 Å, Invar of 47 Å, and aluminum of 53 Å. The roughness of a silicon carbide mirror can be 8–12 Å. These values are after fine polishing. Research indicates that the resulting surface roughness in fine polishing is related to the lubricant used. When using special lubricants, aluminum material can also be polished for optical telescopes. Table 9.1 of Section 9.2.1 lists the surface roughness number of some mirror materials. The requirement for the TIS of an optical mirror surface is around  $10^{-3}$ .

Before the invention of glass ceramics and fused silica, the only material for optical telescope mirrors was borosilicate (BSC) glass. BSC has a relatively high thermal expansion coefficient and is still used for building large honeycomb mirrors. However, borosilicate glass has a very low thermal expansion coefficient

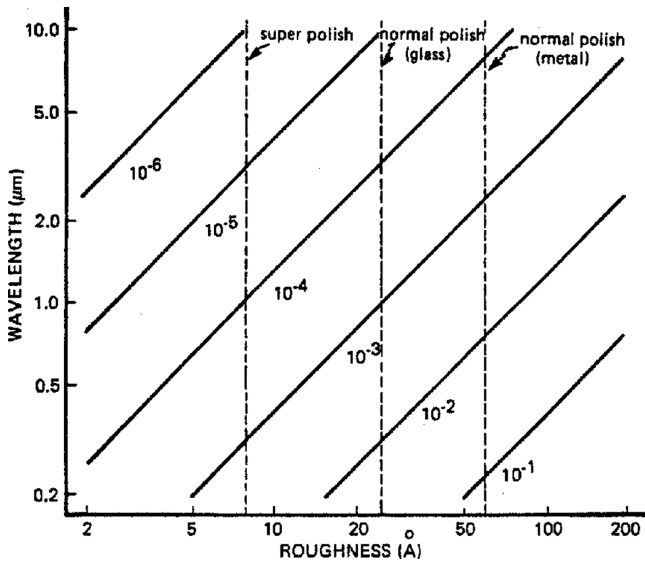
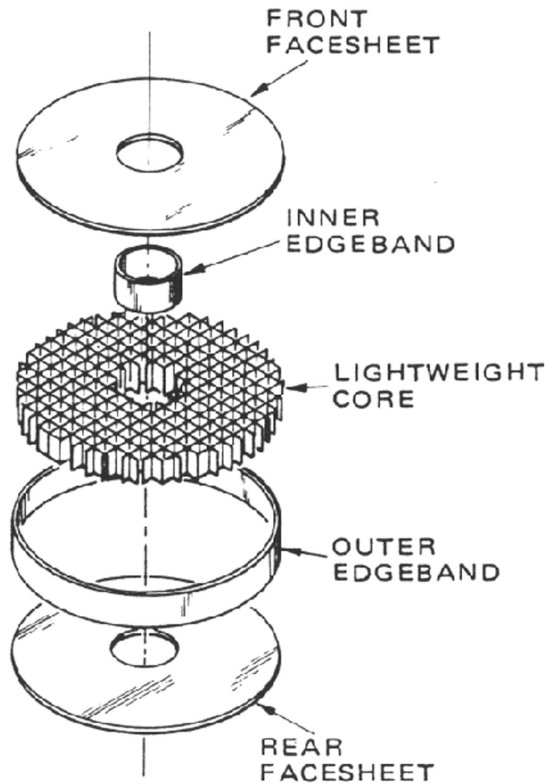


Fig. 2.17. Surface roughness and total integrated scattering.

(about  $0.8 \times 10^{-6} \text{ K}^{-1}$ ) at a low temperature of 40 Kelvins (Section 5.3.2). Therefore, it is a candidate mirror material for modern space infrared telescopes.

Glass ceramic material is made by adding chemical additives (crystal seeds) into liquid glass to germinate fine crystals through thermal treatment. The crystals form a polycrystalline structure with an ultra-low thermal expansion coefficient. However, it is difficult to produce very large, thin, or special shaped glass ceramic mirror blanks due to residual crystallization stresses. It is also not possible to form a honeycomb mirror shape through this casting process.

Another mirror material is fused silica (or fused quartz made from quartz crystals). Fused silica is made by melting naturally high purity silica sand at around  $2,000^\circ\text{C}$  using either an electrically heated furnace (electrically fused) or a gas/oxygen-fuelled furnace (flame fused). Fused silica is translucent or opaque. A large mirror blank can be made by fusing small pieces of blanks together at about  $1,500^\circ\text{C}$ . It is the material for the honeycomb primary mirror of the Hubble Space Telescope. This primary mirror was made of five small pieces: top plate, bottom plate, inner annulus ring, outer annulus ring, and egg-crate core (Figure 2.18).



**Fig. 2.18.** Five components of the HST primary mirror.

Large and very thin primary mirrors of the SUBARU and GEMINI telescopes are also made by fusing hexagonal-shaped fused silica segments. Two steps are used in their manufacture: first to fuse all segments into a flat blank and, second, to soften the blanks into an ideal meniscus shape on a convex mold. Since the mirror is made of several segments, special attention has to be paid in the optimization of thermal distortion. There are small CTE differences between all segments. Different segment arrangement produces different surface rms errors for the same thermal loading. The loading includes absolute temperature change (range about 25°C) and axial temperature gradient (typically 3°C) both in production and in telescope operation. The optimization is through the finite element analysis.

### 2.3.2 Optical Mirror Polishing

Single point diamond turning (SPDT) is an efficient method for the manufacture of metal mirrors. The achievable surface accuracy and roughness using this technique are about 3 and 1  $\mu\text{m}$ , respectively. These mirrors can only be used in the infrared region. They usually do not meet the requirements for large optical mirrors.

To produce glass-type optical mirrors, grinding and polishing are necessary. Four variables affect the removal of mirror surface material in the grinding and polishing process. These are the pressure, the relative speed, the contacting area between the mirror surface and lapping tool, and the abrasive used in the process. Improvement in any of these variables leads to an improvement in the grinding and polishing efficiency. A simplified model assumes linear relationships between the efficiency and any of the first three variables.

Polishing a parabolic surface is much more difficult than polishing a spherical surface because a good surface contact between the tool and the mirror blank is difficult to maintain for a paraboloid shape. The maximum deviation of a paraboloidal surface from a spherical one can be expressed as  $0.00032D^4/F^3$  (where  $D$  is the mirror diameter in meters and  $F$  is the focal length in meters). This expression indicates that the larger the mirror diameter or the smaller the focal length is, the more difficult the mirror polishing will be.

At present, three methods exist in aspherical mirror grinding and polishing. The first one uses traditional grinding tools, the second one uses deformable grinding tools, and the third one involves a pre-stressed mirror blank.

According to the size of the lapping tools used, the first method can be further divided into three sub-classes: one using a full size tool, one using a medium size tool, and one using a small size tool. Using a full size tool to polish a spherical surface is easy. Large-size grinding tools have a large contact area with the blank resulting in high polishing efficiency. However, when the mirror shape departs from a sphere, the contact area required between the tool and the blank at each radius should be different as different amounts of mirror material need to be removed. This requires special contacting patterns on the lapping tool. The

tool pattern is related to the material removed from the mirror and the moving range of the lapping tool.

In general, a full size tool is difficult in polishing an aspherical surface of a small focal ratio. Therefore, a medium size tool is necessary. The medium size tool can remove material of a specific mirror radius. However, one major problem is that the surface under a medium size tool is usually asymmetrical. To correct this, the abrasives can be added only from desirable directions so that the mirror grinding is done in a particular part under the tool, but not in the other parts. This, unfortunately, provides only limited improvement. A small size tool can be easily used to modify the surface shape within a small radius range. Small tools are often used by experienced opticians when polishing large aspherical mirrors. However, care has to be taken as a small size tool introduces high spatial frequency ripples on the mirror surface. These ripples are difficult to remove and to be corrected. Now a small tool with computer control plays a very important role in the modern aspherical mirror fabrication.

A deformable tool can keep a good contact between the tool and the mirror blank when an aspherical surface shape is involved. Two types of deformable tools are used in optical manufacture, passive and active ones. The deformation of a passive tool is from the tool design. There are no external forces or moments applied on the tool except the gravity. When the 4.2 m William Herschel Telescope (WHT) mirror was polished, Brown designed a large full-size polishing tool with a number of deep ring ribs on the tool back. There was no radial rib connection between these rings. The bottom plate of the tool was very thin. With this structural arrangement, the tool was “soft” in the radial direction but “stiff” in the circumferential direction. During the mirror polishing, sandbags are placed on top of the tool to insure a good surface contact between the tool and the blank. Therefore, the contacting area increased and the aspherical surface shape was manufactured.

The active deformable tools involve force and/or moment actuators. The deformation is controlled in real-time through some positional and orientational encoders. R. Angel used an active deformable tool with force actuators for the manufacture of the Vatican  $f/1.0$  primary mirror.

The third polishing method is called stressed polishing where a pre-stressed mirror blank is used instead of an unstressed mirror blank. The mirror shape required under a pre-stressed condition is only a simple spherical shape. However, after the surface has been polished, the desired complex mirror or lens shape can be obtained by releasing the preloaded stresses. The simple surface shape can be a plane or a sphere which is easy to make. The pre-stresses are from either vacuum or force actuators. The method has been used in the manufacture of the off-axis paraboloidal mirror segments of a SMT and the Schmidt corrector plates. Applying this method, iterations and additional corrections using plasma or ion polishing may be needed.

The formulation of pre-stressed polishing of an off-axis conic surface is in Section 2.2.5. For extremely large aperture segmented mirror telescopes, a study shows that the astigmatism is the only important term on the off-axis mirror

segments (TMT design report). Other terms are very small. The astigmatism can be easily eliminated by applying a moment across one mirror diameter. This approach simplifies the stressed mirror blank design for the stressed polishing. After a bending moment has been applied to the mirror blank, the polishing of mirror segments can be done on a planet-type polishing machine. This increases the efficiency and lowers the cost for the mirror segment polishing of an extremely large telescope. A planet-type polishing machine involves a large rotating flat lapping tool and a number of mirror blanks which are floating on top of the tool. Retaining rings (frames) are used to limit the mirror blank's motion so that the blank rotates about both the machine axis and the mirror axis. These two rotational movements produce a uniform material polishing of the mirror surface. If the flat surface tool is replaced by a spherical one, this planet polishing machine can be used for spherical mirror polishing. By putting a stressed mirror blank on top of the spherical tool, the machine can be used for the mass production of off-axis mirror segments for large segmented mirror telescopes. Stressed polishing is a trial and error method for achieving an accurate mirror surface. To avoid iterations, final ion beam polishing or plasma figuring are required.

One problem in mirror polishing is caused by the mirror deformation under the weight of the polishing tool and the mirror itself. To solve this problem, air cushions are used as the mirror support system. In this way, the mirror is floating on the top of the cushions so that the weight of the tool will not produce any local mirror deformation. An air cushion support usually has three axial symmetrical groups of pads arranged in rings. Air valves are used between groups to control the damping of the system. The mirror supported is in the same condition as if it were floating inside a fluid of the same density. This mirror support is called an astatic support.

By using an air-cushion support system the local surface deformation will be very small and it will not influence the surface precision. During the polishing of the UK 1.2 m Schmidt objective prism, a special viscous syrup bag was used for the very thin corrector support. The back side of this Schmidt corrector was glued to the syrup bag and its radial edge was constrained by roller bearings to avoid radial movement. This support arrangement produced a high quality, very-thin Schmidt object prism of 1.2 m size.

Cell print-through is a problem when a honeycomb mirror is under polishing. Honeycomb mirrors have a thin top surface and elastic deformation occurs when the polishing force is applied. This degrades the surface accuracy. To overcome the cell print-through, a special vacuum polishing tool can be used (Figure 2.19). The tool draws air out from the contacting surface between the tool and the mirror to eliminate the force applied on the mirror surface while the removal of mirror material is not affected. Polishing non-spherical surface with magnetorheological fluid or ferro-fluid is a new technique. The viscosity of these fluids can be changed when magnetic field is applied. Therefore, the rate of material removal can be easily controlled.

The ion beam and plasma figurings are also important manufacture methods for astronomical optics. These two methods are mainly used in the final finishing stage of a mirror to achieve precise surface shape modification. The ion beam

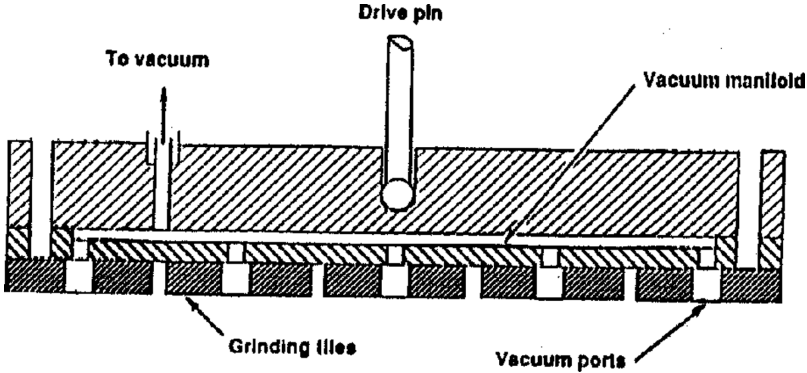
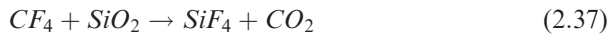


Fig. 2.19. A vacuum polishing tool used for honeycomb mirror manufacture.

figuring is a physical process of bombarding the mirror surface with high speed ions. The mirror should have a low surface roughness before the ion figuring is applied. The whole ion beam process is carried out in a vacuum chamber. The removal of mirror material by ions can be expressed by a beam removal function (BMF). One characteristic of this method is its noncontacting property. So the material removal speed has no relationship with the mirror surface shape. Usually the optical surface is facing down during the ion figuring. This method can achieve a surface precision of about 0.02 visible wavelengths. The main restriction of this method is the dimension of the vacuum chamber.

Plasma polishing is different from ion beam figuring because it is a process of chemical erosion using plasma gas. Some special gas in a plasma state is added in the polishing process, it reacts with the material on the mirror surface. Then the reaction produces active compounds, which detach from the mirror surface. For a fused silica mirror, the reaction is:



The plasma itself has moment in the polishing which will further accelerate the chemical reaction. Plasma polishing can be carried out in a low vacuum condition and it can also produce a high surface precision. It is also a noncontacting polishing method. The efficiency of plasma polishing is higher than that of ion beam figuring.

The discussion in this section was mainly focused on the polishing of astronomical optical surfaces. Other manufacturing methods such as optical surface replications are discussed in Section 2.2.6.

### 2.3.3 Vacuum Coating

Vacuum coating is used to increase the reflectivity of a mirror surface. A metal material is evaporated onto the surface and becomes a thin layer of deposition.

Before the coating, the old film should be removed from the mirror surface. Then the surface is cleaned. The cleaning of the surface is a process of chemical and mechanical reaction. Usually a detergent or a mixture of mild sulfuric and chromic acids is used. After cleaning with acid, the mirror surface should be washed with water. Then the mirror dries in air. Some observatories also use dry ice for the mirror surface cleaning though this process is usually used between coatings to remove dust from the mirror surface.

The coating is done inside a vacuum chamber. The chamber is a large barrel-like container. If the mirror to be coated has a larger dimension, it is usually placed vertically in the chamber. In this position, no metal fuses or other objects will fall on the mirror surface. Metal fuses are arranged at equal distances around the mirror. Then the chamber is evacuated. When the air pressure reaches  $10^{-4}$  to  $10^{-5}$  mmHg ( $1 \text{ mmHg} = 1.33 \times 10^{-2} \text{ Pa}$ ) and can be maintained at this level, the coating process can be started. If a single layer of aluminum film is needed, the coating material, usually aluminum filaments, is placed above a few tungsten heating coils. When the temperature of the filaments is over  $600^\circ\text{C}$ , the aluminum melts and attaches to the heating coils. When the temperature reaches  $1,200^\circ\text{C}$ , the aluminum evaporates. The evaporating aluminum molecules radiate to the mirror and deposit on the surface. In the visible wavelength range, aluminum coating is widely used. For infrared wavelengths, gold or silver has a higher reflectivity. The obvious drawbacks of the silver coating are a low adhesive force and the tendency to oxidize. These can be solved by an additional coating of  $\text{Al}_2\text{O}_3$  or  $\text{SiO}_x$ . Gold, or silver, or platinum are also used for mirrors in X-ray imaging systems.

### 2.3.4 Mirror Supporting Mechanisms

The basic goal of a mirror support is to hold the mirror in the telescope so that the forces of gravity, wind, and telescope acceleration do not significantly change the surface and the position of the mirror. The mirror support includes positioning ones and floating ones. The position of a mirror is defined by a few positioning support points (hard points). The positioning support and its related displacement actuator carry a very small portion of the mirror weight. Most of the mirror weight is carried by “floating” supports to avoid the mirror surface deformation. The floating support is known as astatic flotation which mimics the buoyant force felt if the mirror were floating in a liquid of its own density. The direction of the gravity load of a mirror changes as the elevation changes, so that both axial and radial positioning and floating support systems are used in the mirror support system.

#### 2.3.4.1 Positioning Support Systems for Optical Mirrors

Any rigid body has six degrees of freedom. Therefore, the best mirror support is the so-called “kinematic” mounting, which fixes just six rigid body degrees of



freedom of a mirror. These six degrees of freedom can be applied on a single point, but stresses will be produced around it, or on three or more points. In some cases, the axial and radial positioning points are separately grouped, each with three support points. In some cases, there is no constraint in the mirror axial rotational direction, resulting only five constraints of the mirror positioning system.

Positioning support points can be chosen near the outer edge, or the middle radius, or the inner radius (at the central hole of a primary mirror) of a mirror. In general, the mirror and its cell are made of different materials so that differential thermal expansion may happen when temperature changes. This thermal effect is small when the mirror uses the central hole as its positioning location. The effect will be serious when support radius increases. However, there are two cases where the thermal effect is not a problem even for outer edge positioning. One is when both the mirror and its cell have low CTEs and another is where the positioning constraint degrees of freedom are not affected by the differential thermal expansion.

The HST primary mirror has its positioning device at its outer edge. Above the mirror, the constraint is from a zero-expansion CFRP tube truss. Below the mirror, the constraint is from a low-expansion titanium alloy mirror cell so that the relative movement between the mirror and its positioning device is very small as temperature changes. The advantage of placing the positioning support points on the outer edge is that the mirror will have a higher resonant frequency. For space telescopes, since there is no gravity, the weight of the tube truss would not produce deformation of the mirror when the telescope is in orbit.

For many ground-based telescopes, the mirror cells are made of steel. Radial shear forces may be produced due to differential thermal expansion between the mirror and cell. Therefore, most mirrors use the central hole for positioning location. The position defining points bear little of the mirror's weight. To avoid mirror surface deformation caused by small friction force, the axial and radial contact areas in the central hole positioning system are very small. In the radial direction, the mirror positioning is through a thin tube extended from the mirror bottom support plane. The contacting part is a spherical surface inside the inner mirror hole. To further reduce the contact stress, several vertical slots are made on the sphere surface to absorb any possible stresses.

For mirrors with a small aperture size, the mirror positioning points may be located at the middle radius. These points are on the back of the mirror. This arrangement can be found in a number of secondary mirror support systems. However, if the mirror diameter is not so small, then the force caused by differential thermal expansion remains a problem. An improvement can be made by adding radial flexible springs at the positioning support points. These springs absorb thermal stress between the mirror and its cell.

The three-point mirror support can evolve into a six-point, or nine-point, or more point mirror support through a whiffle-tree design. A whiffle-tree is a beam, or plate, structure, which distributes the support force from one point to two, or three, ends of a beam, or a plate. This force redistribution can be cascaded as a tree structure. However, the degrees of freedom involved are kept the same as a single point support. Differential thermal expansion also exists in a

whiffle-tree support system. To overcome this, the beams which transfer the mirror load to the positioning points should have the same thermal expansion coefficient as the mirror material. Invar is a favorable material used for whiffle-tree beams.

The mirror middle radius positioning is mostly used for mirror axial positioning. The radial mirror positioning is usually at the outer edge of the mirror. Generally three clockwise or anti-clockwise linkage bars in the tangential direction can be used. One end of these linkage bars attaches to the mirror and the other end attaches to the cell. These three tangential linkage bars will fix the mirror in the radial direction. It allows dimensional variation between the mirror and the cell. If the mirror is in zenith position, these linkage bars are free from any loading. When the mirror tilts, the linkage bars will generate a lifting force to counteract the component of the mirror weight along the radial direction. Temperature change and differential thermal expansion have no influence on this type of design. The link bar positioning system allow rotation in axial direction. It constrains only two degrees of freedom.

For very thin mirrors, more positioning support points are required. These support points can also take additional loads, increasing the mirror stiffness, but they will not produce deformation of the mirror surface. These support points are usually equipped with sensors for active or adaptive mirror support force or position control.

A new style of mirror positioning has been developed from the Stewart platform (Parks and Honeycutt, 1998). The basic principle of the six-beam Stewart platform will be discussed in Section 3.1.3. In this hexapod platform,

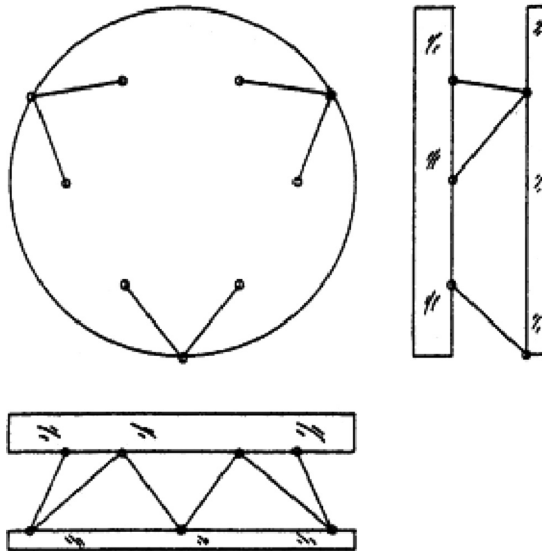


**Fig. 2.20.** Hexapod axial support system for optical mirrors (Parks and Honeycutt, 1998).

each rod has universal joints on both ends. The six rods provide six degrees of freedom for a stable mirror positioning support. Figure 2.20 illustrates a hexapod mirror supporting structure. In this support, the length of each supporting rod is relatively long so that an axial movement of the mirror will be produced when temperature changes. To reduce this temperature effect, the supporting rod can be bent into an 'L' shape so that the distance between the mirror and the cell reduces. If there is a radial force component, a hexapod platform may produce astigmatism of the mirror. Therefore, the hexapod platform support is not an ideal solution for the mirror's radial support.

Parks and Shao extended this hexapod support system to a more complicated 18-point mirror support system. The 18 support points are arranged in two rings. These rings have radii of 0.408 and 0.817 of the mirror radius. Three groups of six points are formed with 12 points at the outer ring and six at the inner ring. One hexapod support device is used for each support group so that the weight of the mirror is evenly distributed to all 18 points. To avoid over-constraint of the mirror, every hexapod platform is connected to a Y-shaped cell with a wire rope in tension. These wire ropes and the connected

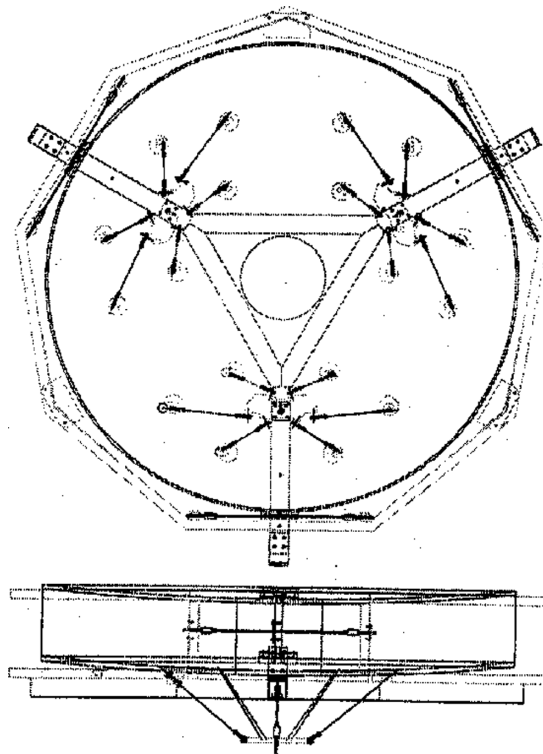


**Fig. 2.21.** An 18-point supporting device and its six-beam linkage subsystem (Parks and Honeycutt, 1998) (Note: Pre-stressed steel wires are used for radial supporting).

hexapods provide a positioning of just six degrees of freedom for the whole mirror and it turns out a very stable mirror support system.

To reduce the support system weight, the lower platforms are made of a triangle truss. In this design, any two of all six rods should not align through one common point for maintaining its stability. Figure 2.21 shows the arrangement of this 18-point hexapod support device. In the radial direction, pre-stressed steel wire ropes are used.

#### 2.3.4.2 Flotation Support Systems for Optical Mirrors

In general, most of the mirror weight is taken up by floating support mechanisms. There are two types of flotation support systems: mechanical and pneumatic ones. A mechanical mirror support system usually involves a counter-weight and cantilever mechanism. The support force generated by this counter-weight and cantilever system follows a sine law of the mirror's elevation angle. This is the same law governing the axial force component change of the mirror weight. Therefore, no force adjustment is necessary in a normal passive support system. The cantilever length ratio produces a magnification of the load applied to the mirror, therefore, the counter-weight required is smaller. The mechanical flotation support system can be used on both axial and radial support. For radial support of a thin mirror, a thin membrane can be used to transfer the support forces from the cantilever system to the support point in radial direction as shown in Figure 2.22. This avoids the effect on the mirror from the bending moment of the system. The main problem of a mechanical flotation support system is the friction involved. It affects thin mirrors.

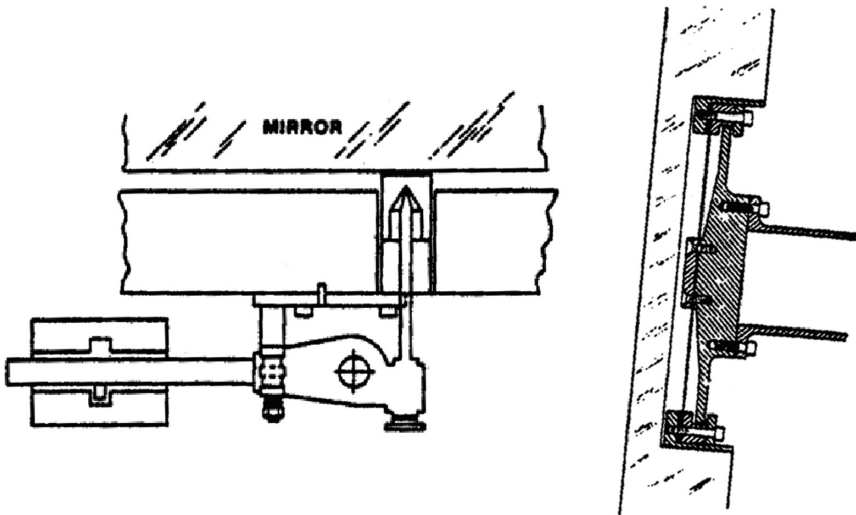


Fig. 2.22. Axial and radial counter-weight and cantilever support systems (Keck).

Air cushions or air cylinders are pneumatic flotation mirror support systems. They are mainly used in axial direction. The support force of these systems is proportional to the mirror contacting area, therefore, the contacting area should remain constant during the telescope operation. The air pressure is adjusted by a pressure regulator so that the required supporting force can be obtained. The regulator follows the motion of the tube to produce sine-law governed air pressure. Force sensors used in the support points may also provide signals to control the air pressure. The air cushions are soft allowing height and tilt adjustments, producing smaller friction forces. When the pneumatic system is not pressurized, the mirror rests on a set of spring-loaded rest pads.

For radial mirror support, a mercury bag is often used. In this system, the mirror is surrounded by a ring-shaped bag filled with mercury. The bag is held by the mirror cell while the mirror floats inside the bag. The force applied on the mirror is proportional to a constant contacting width of the mercury bag.

Another flotation support is a vacuum secondary mirror support system. The principle of a vacuum support is the same as an air cushion system but with a negative air pressure.

In the mirror support system, force sensors can be used to measure the supporting forces. One type of force sensor is the strain gauge. The usage of force sensors is essential for active mirror surface control as discussed in Section 4.1.3.

## 2.4 Mirror Seeing and Stray Light Control

### 2.4.1 Mirror Seeing Effect

Generally, seeing effect is produced by the density inhomogeneities in air along the optical path. Thermal nonuniformities are the main reason behind the air density and air refractive index variation. When a mirror surface has a different temperature from the surrounding air, convection will dissipate these heat nonuniformities. Two types of convection occur over a horizontally placed surface, a natural one and a forced one. Natural convection produces large-scale air bubbles, while forced convection has a thin boundary layer, small scale eddies, and fast time scales (Figure 2.23). The type of air convection can be described by Froude number, which is the ratio of Reynolds number squared to Grashof number, both are introduced in Section 8.1.3 (Dalrymple, 2002):

$$Fr = \frac{Re^2}{Gr} = \left( \frac{VL}{\nu} \right)^2 \frac{\rho \cdot \nu^2}{\Delta \rho g L^3} = \frac{\rho V^2}{\Delta \rho g L} \quad (2.38)$$

where  $V$  is the wind velocity,  $L$  a length scale,  $\nu$  the kinematic viscosity,  $\rho$  the air density,  $g$  the gravity, and  $\Delta \rho$  the magnitude of the density fluctuation of the air.

For  $Fr \gg 1$ , the forced convection dominates; for  $Fr \ll 1$  the natural convection dominates; and for  $Fr = 1$  the convection is mixed. For a heated

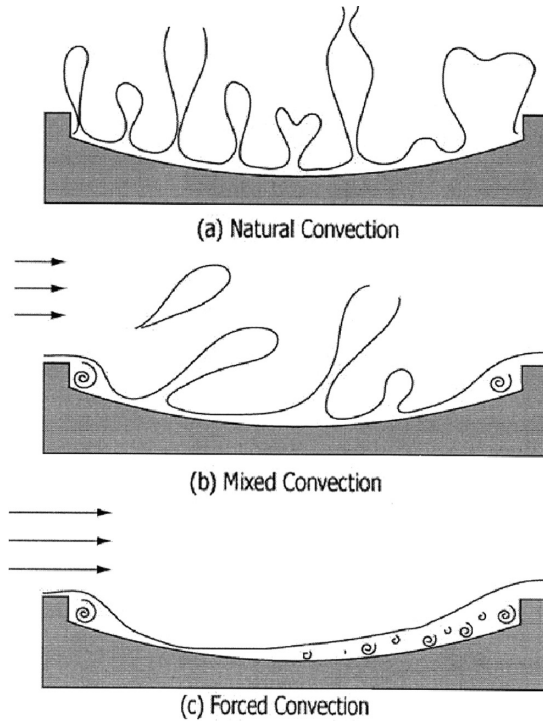


**Fig. 2.23.** Natural and forced convection air flow over the mirror surface (Dalrymple, 2002).

mirror, the length scale is the same as the diameter of the mirror,  $L = D$ . If the air pressure remains constant, then  $\Delta\rho/\rho = \Delta T/T$ , where  $T$  is the temperature and  $\Delta T$  the temperature difference. One can map the convection regimes for particular mirror length scale in wind velocity and temperature difference space base on the Froude number. The Froude numbers between 0.1 and 10 correspond roughly to mixed convection, and higher and lower Froude numbers correspond to forced and natural convection respectively. It is suggested the natural convection produces the most aberration and the forced convection the least.

Air density fluctuation affects optical beams in different ways. For small-scale turbulence, image energy scatters widely and Strehl ratio reduces; for intermediate-scale turbulence, it will produce beam spread and image blurring, resulting in loss of both resolution and contrast; for large-scale turbulence, it will produce tilt-induced image shift, as jitter. A general pattern is a composition of all these three effects. Fast tip/tilt correction can remove jitter (Section 4.1.5). The mirror convection is better kept in the forced convection region, so that the boundaries are smooth and flat.

For a precise expression, the wavefront variance due to the air density change is:

$$\sigma^2 = 2G^2 \int_0^{L_{opt}} \langle \rho'^2 \rangle l_z dz \quad (2.39)$$

where  $G$  is the Gladstone–Dale parameter ( $G = 0.22 \text{ cm}^3/\text{g}$  over the optical wavelength),  $\rho'$  the fluctuating density, which is roughly 10% of the total density variation  $\Delta\rho$  in the air flow,  $\rho' = 0.1\rho\Delta T/T$ ,  $l_z$  the correlation length along the optical axis, and  $L_{opt}$  the total path length through the disturbance. In many cases,  $l_z = 0.1 \sim 0.2L_{opt}$ . The total path length through the disturbance is related to the disturbance layer thickness above the mirror; for natural convection, it is of the scale of the mirror's diameter or larger. The formula of the disturbance layer thickness is:

$$L_{opt} \cong 0.184 \frac{L^{1.5} \Delta T_C^{0.5}}{V} + 0.0392 \frac{L^{0.8}}{V^{0.2}} \quad (2.40)$$

where  $L$  is the upstream heated length (m),  $\Delta T_C$  the average temperature difference over the length ( $^\circ\text{C}$ ), and  $V$  the wind velocity (m/s). For a 4 m diameter mirror in the natural convection case and the wavelength of  $\lambda = 550 \text{ nm}$ , the phase error is about:

$$\phi = \frac{2\pi\sigma}{\lambda} \approx 0.2\pi\rho \cdot G \frac{\Delta T}{T} \frac{\sqrt{2l_z L_{opt}}}{\lambda} \approx 0.48\pi\Delta T \quad (2.41)$$

In the forced convection case, the turbulent flow thickness is much smaller than that of the natural convection. The boundary layer thickness over a flat plate is:

$$\delta = 0.37 \text{Re}_x^{-0.2} x; \quad \text{Re}_x > 10^5 \quad (2.42)$$

and for a velocity of 1 m/s at  $x = 4 \text{ m}$ , this is 12 cm. Higher wind velocity reduces this even further. In general,  $L_{opt} = \delta$ , and  $l_z = 0.1\delta$ . We see that the wavefront error is down from a natural convection case by one to two orders of magnitude.

When the temperature variation is  $\Delta T = 1\text{K}$  for a natural convection case, the wavefront error is small ( $\sigma < \lambda/\pi$ ) and the mirror seeing or the blur angle is:

$$\theta_M = \frac{\theta_D}{\sqrt{S}} \quad (2.43)$$

where  $\theta_D$  is the diffraction limit image angle,  $\theta_D \cong 2.4\lambda/D$ , and  $S$  the Strehl ratio. The Strehl ratio for this weak aberration case is:

$$S \cong \exp \left[ - \left( \frac{2\pi}{\lambda} \sigma \right)^2 \right] = e^{-\phi^2} \quad (2.44)$$

Therefore, the mirror seeing is  $\theta_M \cong 0.2 \text{ arc sec}$ .

In a strong aberration regime, the central core of the point spread function is obscured and the signal is made up of scattered energy and system noise. The blur full angle containing  $p$  percent of the encircled energy is:

$$\theta_{M,p\%} = \frac{4\sigma}{l_z} \sqrt{-\ln(1-p)} \quad (2.45)$$

For  $p = 50\%$ ,  $\theta_{M,50\%} = 3.33\sigma/l_z$ . If the temperature variation is  $\Delta T = 2 \text{ K}$ , the wavefront error is strong ( $\sigma \geq \lambda/\pi$ ) and the mirror seeing is:

$$\theta_{50\%} \cong 0.45 \text{ arc sec} \quad (2.46)$$

Racine's experimental formula of the mirror seeing is:  $\theta = 0.4(T_M - T_e)^{1.2}$ , where  $T_M$  is the mirror temperature and  $T_e$  is the air temperature (Dalrymple, 2002). Figure 2.24 shows the mirror seeing as a function of temperature difference between the mirror and surrounding air.

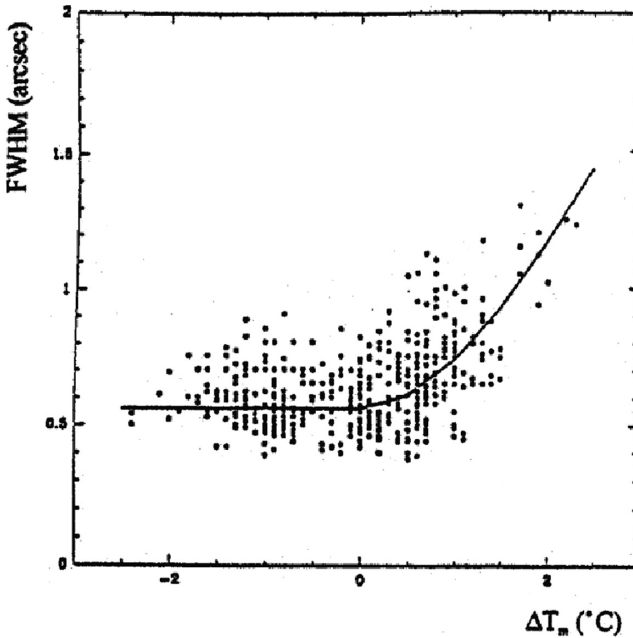


**Fig. 2.24.** Relation between mirror seeing and difference between mirror and air temperatures (Mountain et al., 1994).



### 2.4.2 Stray Light Control

Stray light is any light which does not come from the celestial target sources and yet illuminates the detector. Stray light creates an unwanted background and lowers the sensitivity. For optical telescopes, the source of stray light is the light from celestial objects outside the field of view and the light inside the field of view which does not go to the right position on the focal plane. Both lights are called “off-axis” sources. To overcome stray light, proper design of baffles and stops is necessary. Ray tracing is a way to predict the unwanted stray light. However, for infrared and millimeter wavelength telescopes, thermal emission of the telescope and the surrounding surfaces, including baffles and stops, is a major source of stray light. To overcome these thermal emissions, infrared telescopes may require a design with no baffles in their optical system.

Ray tracing starting from the focal detector is the most effective way of finding and eliminating the stray light in telescopes. In optical system design, ray tracing usually starts from the object space. However, this is not effective in finding stray light in a system. Ray tracing from the detector is like positioning oneself at the detector and looking outward. The first step is to determine the sources which are out of the field of view and still can be seen directly. To block these sources, baffles and stops are required. The next step is to find any object, optical or structural, visible to the detector directly or by the reflection of the optical surfaces. These objects are called “critical objects.” The last step is to find any object, which is seen by the detector and illuminated by stray light sources. These are called “illuminated objects.” If an object is on both the critical and illuminated list, it is on a first-order stray light path. For these objects it is necessary to move them away or to block them. In this way stray light can be reduced by factors of 100 or more. For objects not on the first-order path, the paths with most power must be blocked or removed. However, second-order stray light paths are much more numerous and further ray tracing is necessary.

Stray light ray tracing programs usually use a Monte Carlo approach. A random number generator is used over a selected area, to select only a few random rays to represent all the possible rays in the area, both in position and in direction. In the ray tracing process, each time a ray intersects an object; additional reflected, refracted, and scattered rays are generated. If the secondary rays are shot towards a light source, then the brightness of the surface where the primary ray intersects should be calculated. The power of the primary rays is weighted by the surface scattering rate. This stray light ray tracing is almost the same as the ray tracing in the computer graphical render program. The process is time-consuming because of the intersection calculations. Several approaches can be used to speed up the computations. These are: (a) Use faster computers; (b) Use specialized hardware, especially parallel processors; (c) Speed up computations by using more efficient algorithms; and (d) Reduce the

number of ray-object computations. The ray-object computation reduction includes adaptive depth control, bounding volume, and first-hit speedup.

### 2.4.2.1 Baffle and Stop Design

There are different stops in an optical system. The aperture stop, or the entrance pupil, limits the size of the incoming beam. Objects in the space outside the desired beam are not seen by the detector. The aperture stop is usually the edge of a primary mirror. However, in infrared telescopes, the aperture may be located at the secondary mirror. The field stop limits the field of view. The field stop is located at the focal plane.

Baffles are usually conic or cylindrical tubes designed to block unwanted light paths. To further suppress scattered light, the baffle sides facing the detector may have a series of concentric rings, called “vanes.” For a Cassegrain system, two sets of baffles are required. One is around the secondary mirror, and the other is above the primary mirror as shown in Figure 2.25. The dimensions of the baffles can be found from the following formulae (Bely, 2003):

$$\begin{aligned}
 x_u &= \frac{-b - \sqrt{b^2 - 4ac}}{2a} \\
 r_u &= x_u(\theta - \theta_0) + \theta_0 f_1 \\
 x_l &= \frac{-c_1 b_2 + b_1 c_2}{a_1 b_2 - a_2 b_1} \\
 r_l &= \frac{-c_1 a_2 + c_2 a_1}{b_1 a_2 - b_2 a_1}
 \end{aligned} \tag{2.47}$$

where  $f_1$  is the primary mirror focal length and  $\theta_0$  is the semi-angle one wishes to protect. The other parameters are:

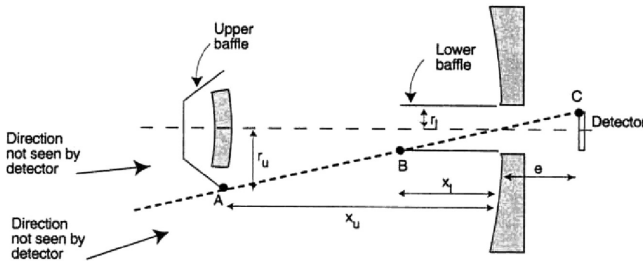


Fig. 2.25. Baffle design for Cassegrain systems (Bely, 2003).

$$\begin{aligned}
\theta_0 &= D/2f_1 \\
a &= \theta_0^2(f_1 + e)^2(m + 1) + \theta_0\theta(f_1 + e)(mf_1(m - 1) - e(m + 1)) \\
b &= -(f_1 + e)^2\theta_0^2((2m + 1)f_1 - e) - \theta_0\theta(f_1 + e)((mf_1)^2 + e^2) \\
&\quad + f_1\theta^2(f_1^2(m^3 - 3m^2) - 2f_1e(m^2 - m) + e^2(m + 1)) \\
c &= \theta_0^2(f_1 + e)^2f_1(mf_1 - e) \\
&\quad - f_1\theta^2((mf_1)^3 + 2f_1^2e(m^2 - m) - f_1e^2(m^2 - m) - e^3) \\
a_1 &= \theta_0(f_1 + e) - \theta(m^2f_1 + e) \\
b_1 &= -(f_1 + e)m \\
c_1 &= \theta_0(f_1 + e)e + \theta(m^2f_1^2 - e^2) \\
a_2 &= \theta_0x_u - \theta_0f_1 - f_1\theta \\
b_2 &= -f_1 \\
c_2 &= -\theta_0f_1x_u + \theta_0f_1^2
\end{aligned} \tag{2.48}$$

where  $D$  is the diameter of the primary mirror and  $m$  is the magnification of the secondary mirror. Baffle surfaces usually have a diffuse black coating to absorb the incoming light. However, none of these coatings will absorb all of the light. At normal incidence, the absorption is a constant. At other angles, surface scattering occurs. When the incident angle is near  $90^\circ$ , the scattering increases to values larger than unity at the specular direction. This scattering can be controlled by placing zigzag vanes to make all the light strike the baffle at a normal incidence.

#### 2.4.2.2 Stray Light Analysis

Specular reflection and scattering are two different but related surface properties in optics. Specular reflection occurs on an ideal reflecting surface or mirror (Figure 2.26). It follows the law of reflection. The optical design is based on specular reflection. The scattering of a surface is described by a bidirectional reflective distribution function (BRDF). BRDF is a ratio between radiation scattered of a unit angular area and surface irradiation weighted with the cosine of the projected

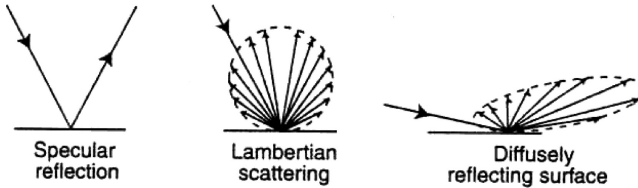


Fig. 2.26. Reflecting and scattering from surfaces (Bely, 2003).

solid angle. For an observer viewing from a different polar angle, the projected solid angle of a surface irradiance area is the solid angle of the area multiplied by a cosine of the polar angle. The expression of BRDF is (Bennett and Mattsson, 1999):

$$BRDF = \frac{dE_s / (Ad\Omega_s \cos \theta_s)}{E_i / A} \approx \frac{E_s / \Omega_s}{E_i \cos \theta_s} \quad (2.49)$$

where  $E_s$  is the radiation over an angular area  $\Omega_s$  with a reflecting angle of  $\theta_s$ ,  $A$  the illuminated area on the surface, and  $E_i$  the surface total irradiation at a point.

If the surface is a perfectly diffuse reflector, light is scattered uniformly, the intensity of the scattered beam varies as the cosine of the angle from the normal of a surface. This is called “Lambertian scattering.” The intensity (the photons per second) is the same for Lambertian scattering which has a constant of  $BRDF = (1/\pi) \text{ sr}^{-1}$ .

An important property of the BRDF is that the half sphere surface integral of the product of BRDF and cosine of the polar angle must be less than or equal to unity. The integration is the reflectance ratio or total integrated scattering of a surface:

$$\int_{\Omega} BRDF \cos \theta \cdot d\Omega = \iint DRDF \cos \theta \sin \theta \cdot d\theta \cdot d\phi \leq 1 \quad (2.50)$$

Another less well-defined parameter is bidirectional scattering distribution function ( $BSDF$ ) which is the scattered power per unit solid angle divided by the incident power:

$$BSDF = \frac{dE_s / d\Omega_s}{E_i} \approx \frac{E_s / \Omega_s}{E_i} \quad (2.51)$$

The BSDF simply uses the cosine-corrected scattered radiance rather than solely the surface irradiance (which has the effect of removing the factor of  $\cos \theta_s$  from the projected solid angle) to yield scatter per unit illuminated surface area per unit solid angle.

All surfaces used in telescopes are in between these two types of scattering. The scattered light is concentrated in the specular direction, but a significant portion of it is around this direction. The flux transferred from a small scattering surface of area  $dA$  into an elementary solid angle  $d\Omega$  can be expressed as:

$$d\Phi = BRDF \cdot E_i dA \cos \theta_i \cos \theta_s d\Omega \quad (2.52)$$

where  $\theta_i$  is the incident angle and  $E_i$  the incident flux density. The BRDF depends on polarization and wavelength. A perfect surface produces specular reflection and has a BRDF infinite in the reflection direction. For lenses and windows, a bidirectional transmission distribution function, BTDF, is used.

When the BRDF of a surface is known, one can calculate the amount of power that is scattered from one surface to another. It is:

$$P_c = \pi \cdot P_s(BRDF)(GCF)$$

$$GCF = A_c \frac{\cos \theta_s \cos \theta_c}{\pi \cdot R_{sc}} \quad (2.53)$$

where  $P_s$  is the incident power on the scattering surface area,  $R_{sc}$  the distance between the scattering and scattered surface area,  $\theta_s$  the scattering angle, and  $\theta_c$  the scattered angle.  $GCF$  is the geometry configuration factor.

The BRDF of a mirror surface is related to the roughness of the surface. However, at infrared wavelengths, dust becomes dominant in scattering. The dust percentage is related to the cleanliness level. It is not practical to have a cleanliness level higher than 500 for large optics. The dust coverage of this level is 1%.

## References

- Bely, P., 2003, The design and construction of large optical telescopes, Springer, New York.
- Bennett, J. M. and Mattsson L., 1999, Introduction to surface roughness and scattering, 2nd edn, Optical Society of America, Washington D. C.
- Cheng, J. and Humphries, C. M., 1982, Thin mirrors for large optical telescope, *Vistas in astronomy*, 26, 15–35.
- Classen, J. and Sperling, N., 1981, Telescopes for the record, *Sky and Telescope*, Vol. 61, Apr. 1981, 303–307.
- Dalrymple, N. E., 2002, Mirror seeing, ATST project report #0003, NOAO.
- ESO, 1986, Very Large Telescope Project, ESO's proposal for the 16 meters very large telescope, Venice workshop, 29, Sep. 2, Oct.
- Hill, J. M., 1995, Mirror support system for large honeycomb mirrors, UA-95-02, Large Binocular Telescope tech memo, steward observatory, University of Arizona.
- Lubliner, J. and Nelson, J., 1980, Stressed mirror polishing. 1 a technique for producing nonaxisymmetric mirrors, *Applied Optics*, 19, 2332.
- Mountain, M. et al., 1994, The Gemini 8 m telescopes project, *SPIE* 2199, 41–55.
- Nelson, J. E., Lubliner, J. and Mast, T. S., 1982, Telescope mirror supports: plate deflection on point supports, UC TMT Report No. 74, The University of California.
- Nelson, J. E., Mast, T. S. and Faber, S. M., 1985, The Design of the Keck observatory and telescope, Keck Observatory Report No. 90, the University of California and California Institute of Technology.
- Parks, R. E. and Honeycutt, K., 1998, Novel kinematic equatorial primary mirror mount, *SPIE* 3352, 537–543.
- Swings, J. P. and Kjar, K. eds., 1983, ESO's Very Large Telescope, Cargese, May.
- West, S. C. et al., 1997, Progress at Vatican Advanced technology telescope, *SPIE Proc.* 2871, 74–83.



<http://www.springer.com/978-0-387-88790-6>

The Principles of Astronomical Telescope Design

Cheng, J.

2009, 634 p. 50 illus., Hardcover

ISBN: 978-0-387-88790-6